Chapter 1
Introduction to Multi-dimensional TCSPC

Wolfgang Becker

Abstract Classic time-correlated single photon counting (TCSPC) detects single photons of a periodic optical signal, determines the times of the photons relative to a reference pulse, and builds up the waveform of the signal from the detection times. The technique achieves extremely high time resolution and near-ideal detection efficiency. The modern implementation of TCSPC is multi-dimensional. For each photon not only the time in the signal period is determined but also other parameters, such as the wavelength of the photons, the time from the start of the experiment, the time after a stimulation of the sample, the time within the period of an additional modulation of the excitation light source, spatial coordinates within an image area, or other parameters which can either vary randomly or are actively be modulated in the external experiment setup. The recording process builds up a photon distribution over these parameters. The result can be interpreted as a (usually large) number of optical waveforms for different combination of the parameters. The advantage of multi-dimensional TCSPC is that the recording process does not suppress any photons, and that it works even when the parameters vary faster than the photon detection rate. Typical multi-dimensional TCSPC implementations are multi-wavelength recording, recording at different excitation wavelengths, time-series recording, combined fluorescence and phosphorescence decay recording, fluorescence lifetime imaging, and combinations of these techniques. Modern TCSPC also delivers parameter-tagged data of the individual photons. These data can be used to build up fluorescence correlation and cross-correlation spectra (FCS and FCCS), to record fluorescence data from single molecules, or to record time-traces of photon bursts originating from single molecules diffusing through a small detection volume. These data are used to derive multi-dimensional histograms of the changes in the fluorescence signature of a single molecules over time or over a large number of different molecules passing the detection volume. The chapter describes the technical principles of the various multi-dimensional TCSPC configurations and gives examples of typical applications.

W. Becker (✉)
Becker & Hickl GmbH, Berlin, Germany
e-mail: becker@becker-hickl.com

W. Becker (ed.), *Advanced Time-Correlated Single Photon Counting Applications*,
Springer Series in Chemical Physics 111, DOI 10.1007/978-3-319-14929-5_1

1.1 Time-Resolved Optical Detection at Low Light Intensity

When light propagates through matter it can interact with the molecules in various ways. In the simplest case, the photons of the incident light may be reflected, absorbed, or scatted. When photons are absorbed the molecules within a sample enter an excited state from which they may return by emitting a photon of longer wavelength. At high intensities several photons may interact with the molecules simultaneously, resulting in nonlinear effects like multiphoton excitation, or second second-harmonic generation. These interactions change the intensity, the spectral properties, and the temporal properties of the light. Light transmitted trough, scattered in, or otherwise emitted from a sample thus carries information on molecular parameters. In other words, optical techniques can be used to probe molecular parameters inside a sample.

Often the effects involved in the conversion of the light are extremely weak, or the concentration of the molecules involved in the conversion processes is low. Moreover, the light intensity tolerated by the sample may be limited. As a result, the intensity of light signals to be detected may be very low. The situation is further complicated when signals are recorded at high time resolution. Optical signals have to be considered a stream of photons. At a given photon rate, the signal-to-noise ratio decreases with the square root of the detection bandwidth. A typical situation is shown in Fig. 1.1. An optical signal was detected by a photomultiplier tube at bandwidth of approximately 350 MHz, or a time resolution of 1 ns. The detected photon rate was approximately 10^7 photons/s. This is much higher than typically obtained in molecular imaging experiments in live sciences. As can be seen from Fig. 1.1, the signal is a random trace of extremely short pulses. The pulses represent the detection of single photons of the light arriving at the detector.

Now consider the detection of a fast optical waveform, such as a fluorescence decay excited by short laser pulses. The fluorescence decay time is on the order of a

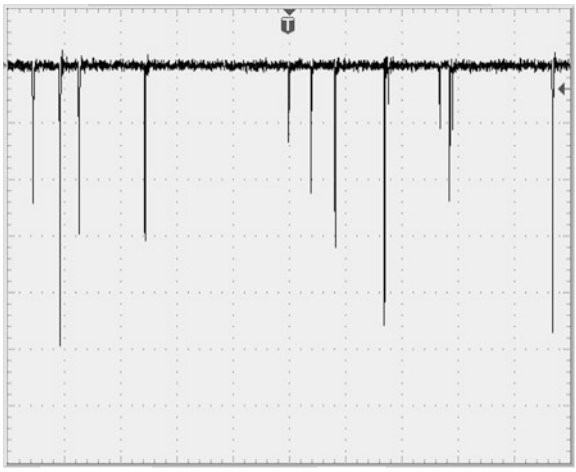

Fig. 1.1 Optical signal detected at a time resolution of 1 ns. Detected photon rate 10^7 photons/s

few nanoseconds. At first glance, it seems impossible to retrieve the signal shape from the signal shown in Fig. 1.1. Nevertheless, there is a solution to the problem: Repeat the experiment, in this case the excitation of the fluorescence decay, for a large number of times, and average the signal detected within a given period of time after the excitation pulses. There is a variety of signal averaging techniques that can be used to recover signals hidden in noise. However, a weak optical signal is special in that it is not a superposition of the signal itself and a noise background. Instead, it is a sequence of individual photon detection events. The signal waveform can therefore more efficiently be reconstructed by determining the arrival times of the photons, and counting them in several time bins according to their times after the excitation pulses.

1.2 Principle of Time-Correlated Single Photon Counting

Time-correlated single photon counting, or TCSPC, is based on the detection of single photons of a periodic light signal, the measurement of the detection times, and the reconstruction of the waveform from the individual time measurements [19, 117]. Technically, TCSPC was derived from the 'Delayed Coincidence' method used in nuclear physics to determine the lifetime of unstable nuclei. The earliest publication on the use of the method to detect the shape of light pulses dates back to 1961 [34], the first applications to spectroscopy of excited molecules were published in the 1970s [50, 96, 97, 133, 151].

TCSPC makes use of the fact that for low-level, high-repetition rate signals the light intensity is usually low enough that the probability to detect more than one photon in one signal period is negligible. The situation is illustrated in Fig. 1.2.

Fluorescence of a sample is excited by a laser of 80 MHz pulse repetition rate (a). The expected fluorescence waveform is (b). However, the detector signal, (as measured by an oscilloscope) has no similarity with the expected fluorescence

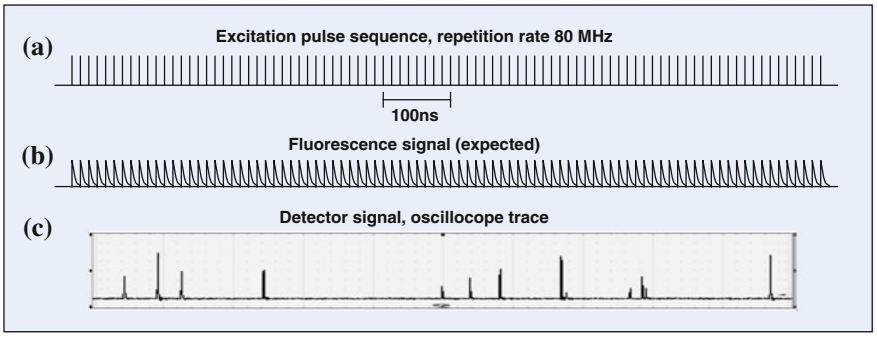

Fig. 1.2 Detector signal for fluorescence detection at a pulse repetition rate of 80 MHz. Average photon rate 10^7 s^{-1}

waveform. Instead, it is a sequence of extremely narrow pulses randomly spread over the time axis (c). A signal like this often looks confusing to users not familiar with photon counting. Of course, there is a simple explanation to the odd signal shape: The pulses represent single photons of the light signal arriving at the detector. The shape of the pulses has nothing to do with the waveform of the light signal. It is the response of the detector to the detection of a single photon. Please note that the photon detection rate of (c) was about 10^7 s^{-1}. This is on the order of the maximum permissible detection rate of most photon counting detectors. Even at a detection rate this high, the detector signal is far from being a continuous waveform.

There are two conclusions from the signal shape in Fig. 1.2c. First, the waveform of the optical signal is not the detector signal. Instead, it is the distribution of the detector pulses over the time in the excitation pulse periods. Second, the detection of a photon within a particular excitation pulse period is a relatively unlikely event. The detection of two or more photons is even more unlikely. Therefore, only the first photon within a particular pulse period has to be considered. The build-up of the photon distribution over the pulse period then becomes a relatively straightforward process. The principle is shown in Fig. 1.3.

When a photon is detected, the arrival time of the corresponding detector pulse in the signal period is measured. The event is transferred into a digital memory by adding a '1' in a memory location proportional to the measured detection time (Fig. 1.3a). The same is done for a second photon (Fig. 1.3b). The process is continued until a large number of photons has been detected and accumulated in the memory (Fig. 1.3c). The result is the distribution of the photons over the time after the excitation pulses. The distribution represents the 'waveform' of the optical pulse (Please note that there is actually no such waveform, only a distribution of the photon probability, see Fig. 1.2). The principle is similar to the 'delayed coincidence' method used in nuclear physics to record the decay times of unstable nuclei. TCSPC has, in fact, been derived form the techniques used there [34, 110].

Although the principle of TCSPC looks complicated at first glance, it has a number of intriguing features. The first one is that the time resolution is better than the width of the single-electron response (SER) of the detector. The explanation is given in Fig. 1.4. The times of the photons are derived from the arrival times of the detector pulses. These times can be measured at an accuracy much better than the width of the pulses. Thus, the 'instrument response function', or IRF, of a TCSPC system is essentially given by the transit time dispersion (or transit time spread, TTS) of the photon pulses in the detector. The TTS can be more than 10 times shorter than the single-photon response of the detector. The IRF is therefore much narrower than the detector response. This is a considerable advantage over techniques based on direct analog recording of the detector signal [19, 117].

The second advantage is that there is no loss of photons in the recording process. Provided the timing electronics is fast enough every photon seen by the detector arrives in the photon distribution. TCSPC therefore reaches a near-ideal counting efficiency [83]. In particular, the efficiency is much higher than for recording techniques that shift a time-gate over the optical waveform [19, 120].

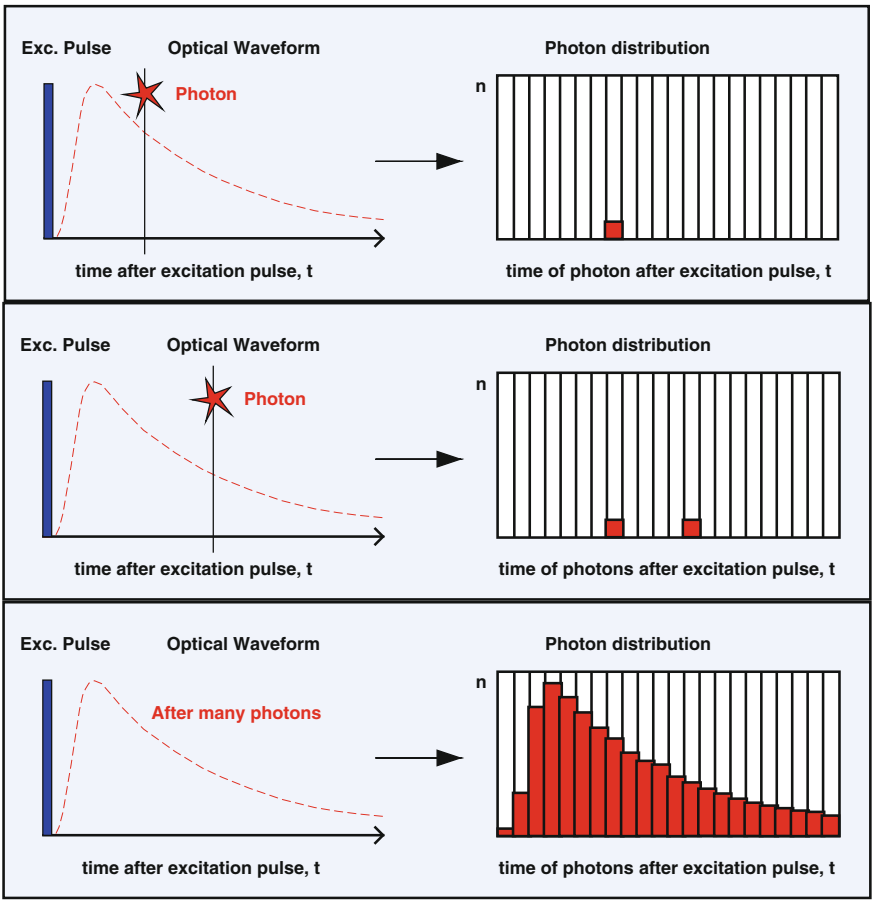

Fig. 1.3 Principle of TCSPC: the recording process builds up the distribution of the photons over the time after the excitation pulses

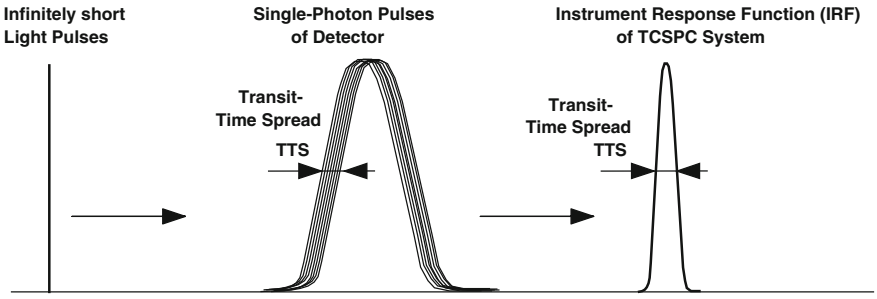

Fig. 1.4 Response of detector to infinitely short light pulses and instrument response of TCSPC system

There is also a third advantage that has been noticed only recently. If there is variation in the optical signal waveform over the time the data are acquired TCSPC records an *average waveform*. This can be important in biomedical applications where the optical waveforms may vary due to metabolic processes. A technique based on temporal scanning, i.e. by shifting a time-gate over the signal, would record a distorted waveform in these cases.

As a serious drawback of TCSPC it is often stated that the technique can record only one photon per signal period. If the light intensity is high a possible second or third photon in the same excitation pulse period with the first one is lost. The result is a distortion of the recorded signal waveform. Pile-up was indeed a serious problem in early TCPC experiments working at pulse repetition rates on the order of 10 kHz. It is far less a problem in modern implementations which work at pulse repetition rates on the order of 50–80 MHz. A derivation of the systematic error in the detected fluorescence lifetime has been given in [19]. For detection rates not exceeding 50 % of the excitation rate the measured intensity-weighted lifetime, τ_{meani}, of a single-exponential decay of the true lifetime τ can be approximated by

$$\tau_{meani} \approx \tau \ (1 - P/4)$$

P is the average number of photons per excitation period. The ratio of the recorded lifetime, $\tau_{meani,}$ and the true lifetime, τ, as a function of the average number of photons, P, is shown in Fig. 1.5. The lifetime error induced by pile-up is surprisingly small: Even for an average detection rate of 20 % of the excitation rate ($P = 0.2$) the lifetime error is no larger than 5 %. For excitation with a Ti:Sa laser (80 MHz) $P = 0.2$ would correspond to a detection rate of 16 MHz. This is much more than the detection rates in typical TCSPC experiments. With state-of-the-art laser sources and TCSPC electronics the count rate—and thus the available acquisition speed—is rather limited by the photostability of the samples than by pile-up effects [22]. This is especially the case in fluorescence lifetime microscopy where the fluorescence comes from a pico- or femtoliter sample volume.

The real limitation of the classic TCSPC principle is that it is *intrinsically one-dimensional*. That means, it records only the *waveform* of the signal. To record, for instance, the fluorescence decay function for a range of wavelengths, or over the

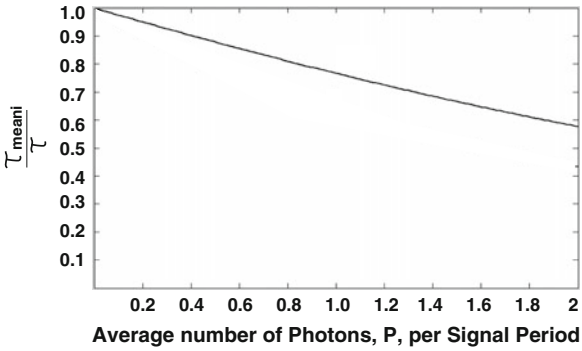

Fig. 1.5 Ratio of measured intensity-weighted lifetime, τ_{meani} and the true lifetime, τ, as a function of the number of photons, P, detected per signal period

pixels of an image area, the decay functions had to be recorded sequentially for a series of wavelengths or for the individual pixels of the image.

In applications were only a single optical waveform has to be recorded, or the experiment allows a series of waveforms to be recorded sequentially the classic principle is still used to a large extend. The typical application is recording of fluorescence decay curves. Examples are shown in Fig. 1.6. Figure 1.6, left, shows fluorescence decay curves of quinine sulphate quenched by Cl^- ions. The fluorescence lifetime changes with the quencher concentration [92]. Figure 1.6, right shows decay curves of DODCI (3,3′diethyloxadicarbocyanine iodide) for different wavelength. The data were obtained by scanning the detection wavelength by a monochromator and recording the decay curves sequentially.

The classic TCSPC principle is often used to record fluorescence anisotropy decay times. A sample is excited by linearly polarised light, and the fluorescence decay function measured in two directions of polarisation. An example is shown in Fig. 1.7. Fluorescein in a water-glycerol solution was excited at 474 nm. The blue curve shows the fluorescence decay measured at a polarisation parallel, $I_{par}(t)$, the red curve the fluorescence decay at a polarisation perpendicular to the excitation, $I_{perp}(t)$. The black curve shows the anisotropy, $R(t)$, (arbitrary units) calculated by

$$R(t) = I_{par}(t) - I_{perp}(t)/I_{tot}(t)$$

$I_{tot}(t)$ is the total intensity. For measurement in a 90° parallel-beam configuration it is $I_{tot}(t) = I_{par}(t) + 2\ I_{perp}(t)$ [92, 144], for excitation and detection from the full half space it approaches $I_{tot}(t) = I_{par}(t) + I_{perp}(t)$ [22]. Please see also Chaps. 3 and 12.

The problem of anisotropy-decay measurement is that noise and systematic errors in the difference $I_{par}(t) - I_{perp}(t)$ are much larger than in the signals themselves. Therefore, high-accuracy data are required which can only be obtained by TCSPC. Please see Chap. 12 for details.

The advantage of fluorescence-anisotropy experiments is that the anisotropy decay time bears information on the size of the fluorophore molecule, possible binding to other molecules, and on the viscosity of the molecular environment. It is therefore used to investigate the configuration of fluorescence-labelled bio-molecules. Such

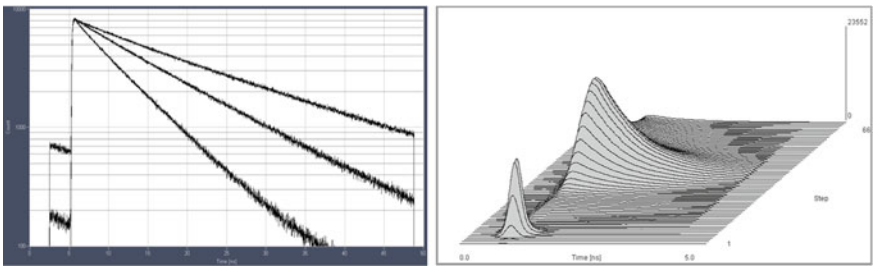

Fig. 1.6 Fluorescence decay measurement by TCSPC. *Left* Fluorescence decay curves of quinine sulphate for different quencher concentration. *Right* Fluorescence decay curves of DODCI recorded for different wavelengths

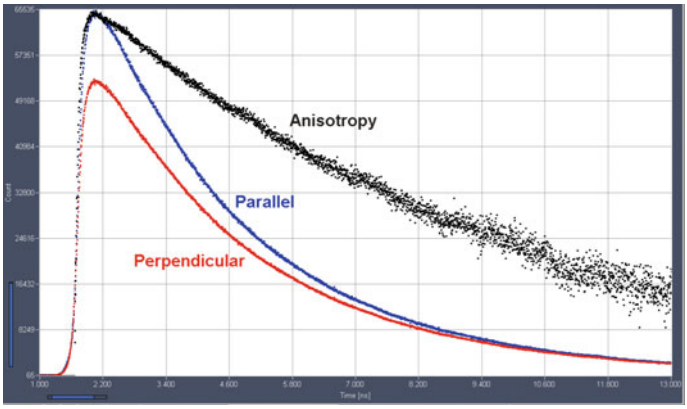

Fig. 1.7 Fluorescence anisotropy measurement. The fluorescence of a sample was measured at polarisation angles of 0° and 90° to the polarisation of the excitation; the anisotropy was calculated by $R(t) = I_{par}(t) - I_{perp}(t)/I_{tot}(t)$

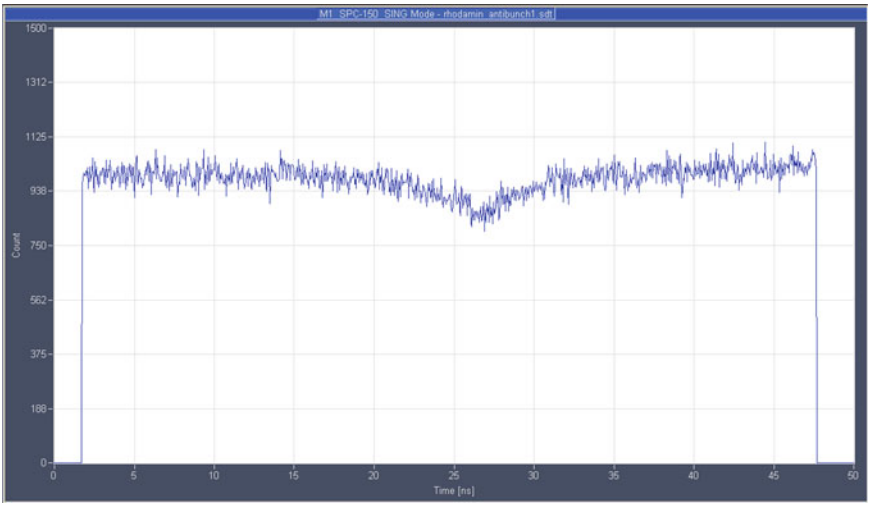

Fig. 1.8 Anti-bunching curve recorded at a diluted solution of fluorescein in a confocal microscope. About 7 molecules are in the focus at a time

experiments and their interpretation can be real detective stories [93, 94, 114, 115, 132, 142].

Another application of the classic principle is recording of anti-bunching effects. A single optical emitter, such as a single molecule or a quantum dot, can only emit a single photon within its fluorescence decay time. The experiment is run in the classic 'Hanbury-Brown-Twiss' setup [72]: The light is split in two detection channels, and the detection events in one detector are used as a start, the ones in the

other as a stop signal for TCSPC. The resulting curve has a dip at a time at which the events coincide. Two examples are shown in Fig. 1.8.

Until today, some of these basic applications are performed by TCSPC setups based on the classic NIM (Nuclear Instrumentation Module) architecture [117]. Of course, modern TCSPC devices (see below) have the traditional recording modes implemented as well. Even in simple applications as the ones shown above the modern devices have advantages over NIM-based instruments: They work at higher pulse repetition rates and higher count rates, achieve shorter acquisition times, and are fully computer controlled. The real advantage of the modern implementation is, however, that the recording process is multi-dimensional. As a result, experiments can be performed which are entirely out of the reach of the classic design.

1.3 Multi-dimensional TCSPC

1.3.1 Principle of Multi-dimensional Recording

Development of multi-dimensional TCSPC goes back to the realisation that TCSPC records a photon distribution. In case of classic TCSPC, the distribution is over only one parameter, which is the time after an excitation pulse. However, if, by any means, additional parameters can be associated to the individual photons, the photon distribution can be made multi-dimensional. Typical parameters are the wavelength of the photons, the time from the start of an experiment, the distance along a one-dimensional scan, or the spatial coordinates within an image area. The difference between classic TCSPC and multi-dimensional TCSPC is illustrated in Fig. 1.9.

Depending on which and how many additional parameters are used, different photon distributions are obtained. Three possibilities are shown in Fig. 1.10. Wavelength-resolved fluorescence decay data (shown left) are obtained by using the wavelength as additional recording parameter. Dynamic fluorescence decay data (middle) are obtained by using the time from a stimulation event. Fluorescence lifetime imaging (right) uses the spatial coordinates, x, y, within an image as additional parameters.

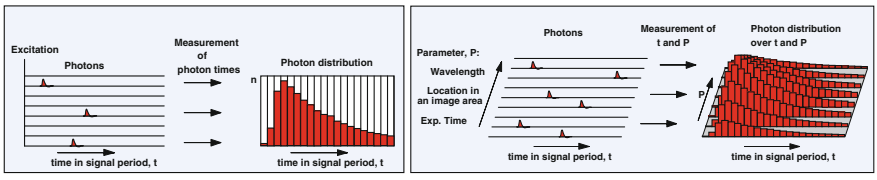

Fig. 1.9 *Left* Principle of classic TCSPC. The result is a one-dimensional photon distribution over the time in the signal period. *Right* Multi-dimensional TCSPC. The result is a multi-dimensional distribution over the time in the signal period and one or several additional parameters determined for the individual photons

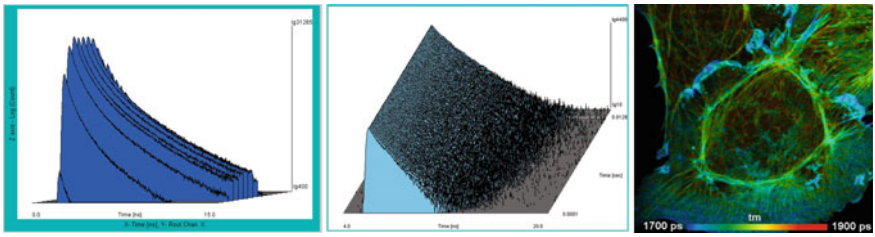

Fig. 1.10 Examples of photon distributions recorded by multidimensional TCSPC. *Left to right* Wavelength resolved fluorescence decay, dynamic change of fluorescence decay after a stimulation of the sample, fluorescence lifetime image obtained by fast confocal scanning

It is sometimes believed that the same results an also be obtained by classic TCSPC if only the parameter of interest would be varied and a sequence of waveforms be recorded. This is correct, but there is an important difference. The classic procedure would have to acquire a full waveform until the value of the parameter is changed, and then start a new recording. That means, any change in any of the additional photon parameters had to be slow, and predictable.

Multi-dimensional TCSPC is free of this limitation. Any parameter of the photon distribution can vary at any speed. It can even vary randomly. Every photon is just put into its place in the photon distribution according to its time after the excitation and the value of the additional parameters in the moment of the photon detection. As the parameters keep varying, the photon distribution is just accumulated until enough photons have been collected for any particular combination of parameters. In other words, the rate at which the parameters are varying is decoupled from the rate at which the photons are recorded.

Typical examples are the results shown in Fig. 1.10: The wavelength of the photons in Fig. 1.10 was determined by a multi-wavelength detector. It varies randomly, and is different for every photon. The variation in the fluorescence decay functions in Fig. 1.10, middle, is induced by repetitive stimulation of the sample. The data were accumulated over a large number of stimulation periods. Thus, a high signal-to noise ratio was obtained despite of the fact that the variation in the decay curves was recorded at a resolution of 100 µs/curve. The lifetime image on the right was recorded by scanning the sample with a pixel dwell time of one microsecond. At an average photon rate on the order of 10^6 s^{-1} one would expect that the result would contain no more than a few photons per pixel. Fluorescence decay data acquired this way would be useless. However, because the photons were accumulated over a large number of frames of the scan, an excellent accuracy of the decay time is obtained.

Despite of its large potential the idea of multidimensional TCSPC has spread only slowly. The introduction was hampered by the fact that the principles behind TCSPC in general and multi-dimensional TCSPC in particular were not commonly understood. The first patent dates back to 1998 [8], a paper at least partially related to multidimensional TCSPC was published in 1991 [9], and two other patents followed in 1993 [10, 11]. The first multidimensional-TCSPC devices on the

market were the SPC-300 and SPC-330 boards of Becker & Hickl. These boards had memory space for up to 128 waveforms. The SPC-430 boards introduced in 1994 already had space for up to 2048 waveforms, and had fast time-series recording and parameter-tag functions for single-molecule spectroscopy [12, 121]. The first TCSPC module with imaging capability was the SPC-535 introduced in 1995. The final breakthrough came in 2001 with the introduction of TCSPC FLIM into fluorescence laser scanning microscopy [13–16].

1.3.2 Architecture of TCSPC for Multidimensional Data Acquisition

The general architecture of a TCSPC device with multi-dimensional data acquisition is shown in Fig. 1.11, left.

The core of the TCSPC device is the time measurement block. This block receives the single-photon pulses from a detector, and the timing reference pulses from a pulsed light source. The time is measured from a start pulse to a stop pulse. Depending on the principle used in the timing electronics the time between start and stop can be measured at an accuracy from about 20 ps (rms) down less than 3 ps (rms). Please see [19] for technical details.

In early TCSPC applications the start pulse came from the light source, the stop from the detector. When high-repetition rate lasers were introduced as light sources start and stop has been reversed: The time measurement is started with the photon, and stopped with a reference pulse from the light source. This 'reversed start-stop' principle has the advantage that the timing electronics need not work at the high repetition rate of the light source but only at the much lower photon detection rate. Please see [19] or [22] for technical details.

The time measurement block delivers the photon time, t, relative to the stop pulse as a digital data word. The data word addresses the time-channel in a selected waveform data block in the memory. The photon is added in the addressed memory location. As more and more photons are detected the waveform of the optical signal builds up.

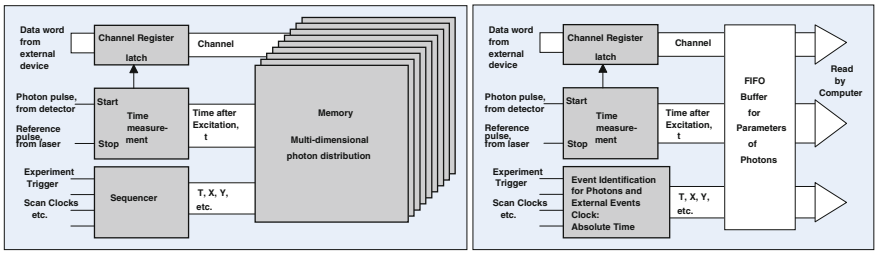

Fig. 1.11 Multi-dimensional TCSPC architecture. *Left* Photon distribution built up in memory of TCSPC device. *Right* Photon distributions built up in computer

Up to this point the function of the TCSPC device is identical with classic TCSPC. The difference is, however, that the memory has space for a large number of waveform data blocks, and that these blocks can be addressed via additional building blocks of the TCSPC device. The address part delivered by these blocks carries additional information related to the individual photons. Photon parameters available directly as digital data words are fed into the TCSPC device via the 'Channel' register. Examples are the wavelength channel in which a photon was detected by a multi-wavelength detector (see Sect. 1.4.1), or the number of one of several multiplexed lasers or laser wavelengths (see Sect. 1.4.2). The external data word is read into an the 'Channel' register in the moment when the corresponding photon is detected.

Additional parts of the address can be generated by a 'Sequencer' block. The sequencer generates an address word either by counting synchronisation pulses from an external experiment control device (e.g. an optical scanner), or by counting pulses from an internal clock.

Figure 1.11, left, the photon distributions are built up by on-board logics in the memory of the TCSPC device. The advantage of this principle is that the acquisition runs virtually without interaction of the measurement control software.

A second architecture is shown in Fig. 1.11, right. Here, the parameters of the individual photons are directly transferred into the system computer. To buffer the information for periods when the computer is not able to read the data a FIFO (first-in-first-out) buffer is inserted in the data path. The computer builds up the photon distribution by software or directly stores the data of the individual photons for further processing.

When data of individual photons are generated there is no need to use a sequencer to direct photons into different waveform data blocks of the memory. The function of the sequencer is therefore performed by 'Event Identification' logics. This block adds an absolute time (from the start of the recording) to the data words of the individual photons. Moreover, it puts external events, such as trigger pulses from an experiment or synchronisation pulses from a scanner, into the data stream and marks them with an absolute time and an identifier.

The advantage of this architecture is that more memory size is available to build up the photon distributions, and that more complex data operations can be performed. Because the principle in Fig. 1.11, right, uses a stream of data for photons marked with detection times and other parameter it is also called 'time tag' or 'parameter-tag' mode.

1.4 Multidimensional TCSPC Implementations

The system architecture shown in Fig. 1.11 can be used for a wide variety of recording tasks. Depending on the information fed into the TCSPC module photons can be recorded versus the time after the excitation, detection wavelength, excitation wavelength, distance along a line scan, coordinates in a scan area, excitation and

detection positions multiplexed by a fibre switch, time from a stimulation of the sample, or time within the period of an additional modulation of the excitation laser. Photon distributions can be built up over almost any combination of these parameters. The photon data can be processed internally by the architecture shown in Fig. 1.11, left, or externally by the architecture shown in Fig. 1.11, right. A comprehensive description of all combinations would be out of the framework of this book. The sections below therefore concentrate on frequently used implementations.

1.4.1 Multi-detector and Multi-wavelength TCSPC

Multidimensional TCSPC is able to detect several optical signals simultaneously by several detectors. Although the principle can be used to record any signals originating from the same excitation source the main application is multi-wavelength TCSPC. The principle of multi-wavelength TCSPC is illustrated in Fig. 1.12. The light is dispersed spectrally, and the spectrum is projected on an array of detectors. The detector electronics determines the detector channel at which a particular photon has arrived. The channel number thus represents the wavelength of the photon. It is used as a second dimension of the photon distribution. The result is a photon distribution over time and wavelength.

To understand why multi-wavelength detection works, please remember that the average number of photons detected per signal period is far less than one, see Fig. 1.3. It is therefore unlikely that several photons per signal period will be detected. Now consider an array of detectors over which the same photons flux is dispersed spectrally. Because it is unlikely that the complete array detects several photons per period it is also unlikely that several detectors of the array will detect a photon in one signal period. This is the basic idea behind multi-detector TCSPC. Although several detectors are *active simultaneously they are unlikely to deliver a photon pulse in the same signal period*. Therefore, only single detection events in one of the detector channels have to be considered. Consequently, the times of

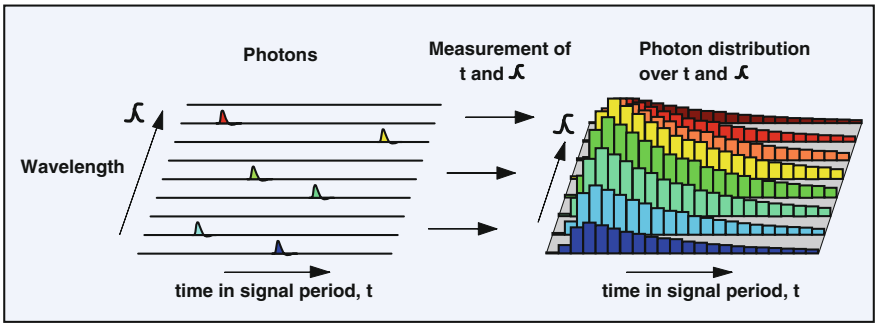

Fig. 1.12 Multi-wavelength TCSPC determines the wavelengths of the individual photons and builds up a distribution over the arrival time in the signal period and the wavelength

the photons detected in all detector channels can be measured by a single time-measurement block [11, 19, 22].

The technical principle is illustrated in Fig. 1.13. The photons of four detectors are combined into a common timing pulse line. Simultaneously, a 'Channel' signal is generated that indicates in which of the detectors a particular photon was detected. The combined photon pulses are sent through the normal time measurement procedure of the TCSPC device. The detector number is used as a 'channel' signal for multi-dimensional TCSPC. Considered from the point of view of multi-dimensional TCSPC the TCSPC device builds up a photon distribution over the times of the photons after the excitation and the detector channel number. Because the individual photons are routed into different memory blocks according to the detector in which they were detected the technique has been called 'routing', and the device that generates the channel number 'router'.

Routing has already been used in classic NIM-based TCSPC setups [27, 140]. Each of the detectors had its own constant-fraction discriminator (CFD). The CFD output pulses were combined into one common TAC stop signal, and simultaneously used to control one or two higher address bits of the multichannel analyser. Because separate CFDs were used for the detectors, the number of detector channels was limited. The modern implementation uses a single CFD for all detector channels, as shown in Fig. 1.13. The 'router' combines the single-photon pulses into one common timing pulse line, and generates a channel signal that indicates at which of the detectors the current photon arrived, see Fig. 1.13.

Routing is often used in time-resolved anisotropy decay measurements. An advantage in this application is that the photons for parallel and perpendicular polarisation are processed in the same timing electronics and are thus recorded at exactly the same time scale. In other applications with no more than four channels routing systems are more and more replaced with fully parallel TCSPC systems [21, 76]. Routing is used, however, to further extend parallel TCSPC systems and to obtain large detection channel numbers with single TCSPC modules. Typical applications are diffuse optical imaging by near-infrared spectroscopy (NIRS) and multi-wavelength TCSPC. NIRS systems with up to four TCSPC channels and 32 detectors (8 for each TCSPC channel) are used [48, 49]. Multi-wavelength TCSPC

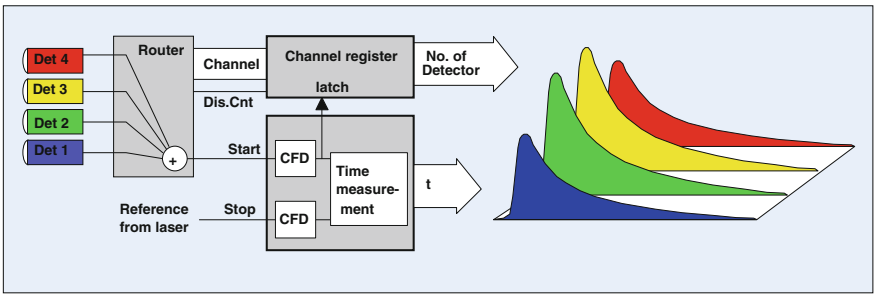

Fig. 1.13 TCSPC multidetector operation, several individual detectors. By the 'channel signal' from the router, the photons of the individual detectors are routed into separate memory blocks

with 16 spectral channels is used in tissue spectrometers (see below) and in fluorescence lifetime imaging systems (see Sect. 1.4.5.2).

The architecture of a multi-wavelength TCSPC system is shown in Fig. 1.14.

A spectrum of the light to be recorded is projected on the photocathode of a multi-anode PMT. The routing electronics and the multi-anode PMT are integrated in a common housing. The combination of the photon pulses of all channels is achieved by deriving the pulses from the last dynode of the PMT [19, 22].

The high counting efficiency and the elimination of any wavelength scanning makes multi-wavelength TCSPC attractive to biological and biomedical applications. A typical setup of a multi-wavelength tissue lifetime spectrometer is shown in Fig. 1.15. It consists of a picosecond diode laser, a fibre probe, a polychromator, a 16-anode PMT with routing electronics, and a TCSPC module. [19, 22]. Multispectral fluorescence decay data of human skin obtained this way are shown in Fig. 1.15, right.

A portable instrument of this type has been described by De Beule et al. [51]. It uses two multiplexed ps lasers of 355 and 440 nm wavelength. Recording of the multiplexed signals was obtained by the technique described in Sect. 1.4.2. The results have 32 decay-curve channels for different combinations of excitation and detection wavelength.

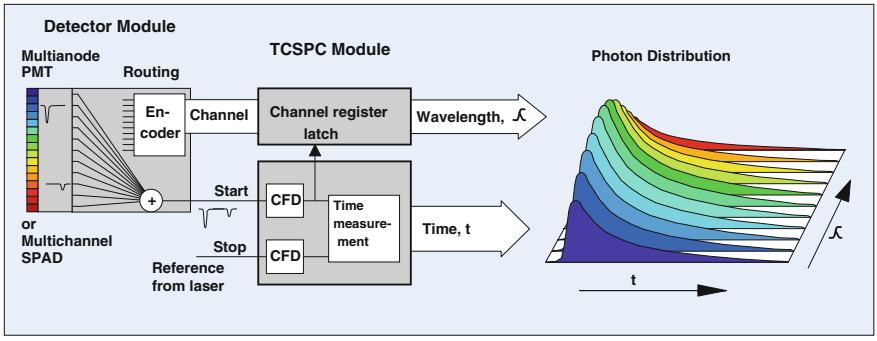

Fig. 1.14 Multi-wavelength TCSPC

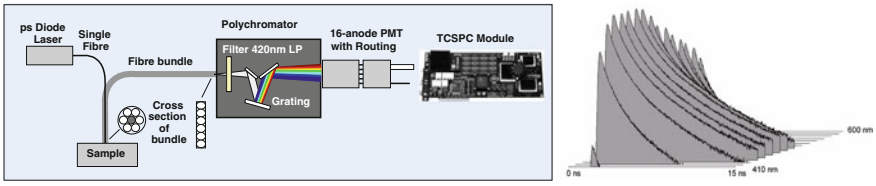

Fig. 1.15 *Left* Optical setup for single-point autofluorescence measurement. *Right* Multi-wavelength fluorescence decay data of human skin. Time scale 0–15 ns, wavelength scale 410–600 nm, intensity scale logarithmic from 500 to 30,000 counts/channel

Other non-scanning multi-wavelength TCSPC applications use a micro-spectrometric setup with a microscope and a confocal detection beam path to obtain fluorescence from a specific location within a cell [40].

Most multi-wavelength applications target at the measurement of the metabolic state of cells and tissue. Information is obtained from the fluorescence decay functions of NADH and FAD, see Chaps. 13, 14 and 15. Extracting accurate decay parameters is, however, difficult because both the excitation and the emission spectra of NADH and FAD overlap. Spectrally resolved detection of decay parameters therefore helps separate the individual decay components [40, 41, 46, 153]. An overview on multi-wavelength detection of NADH and FAD has been given by Chorvat and Chorvatova [42]. Using a micro-spectrometry setup, Chorvat et al. found changes in the decay signature during rejection of transplanted hearts in human patients [43]. The effect of Ouabain on the metabolic oxidative state in living cardiomyocytes was shown in [44], the effect of oxidative stress in [45].

De Beule et al. used a tissue spectrometer setup and demonstrated the applicability of NADH and FAD multi-wavelength lifetime imaging to cancer detection and diagnosis [51]. Using a similar optical setup Coda et al. found significant differences in the fluorescence lifetime of normal and neoplastic tissue [47].

Multi-wavelength detection becomes even more attractive when its is combined with fluorescence lifetime imaging microscopy [15, 19, 20, 22]. Please see Sect. 1.4.5, and Chap. 2 of this book.

1.4.2 Excitation Wavelength Multiplexing

The routing capability of TCSPC can be used to multiplex several light signals and record them quasi-simultaneously [9, 19]. The most common application of multiplexed TCSPC is recording of fluorescence signals excited by several multiplexed lasers. Each laser is turned periodically for a short period of time, and a routing signal is generated indicating which of the lasers is active at a given time. The routing signal is used to identify the photons excited by different lasers, and to store them in different waveform blocks of a common photon distribution. The principle is shown in Fig. 1.16.

Excitation wavelength multiplexing is easy with picosecond diode lasers. Diode lasers can be turned on and off electronically at a speed in the ns range. Multiplexing can also be implemented elegantly by using a super-continuum laser with an acousto-optical filter (AOTF). The transition from one filter wavelength to another takes only a few microseconds. All that is needed to multiplex several lasers or filter wavelengths is a simple controller that generates the on/off selection signal to the diode lasers or to the AOTF, and the routing signal to the TCSPC device. Please see Chap. 18.

Laser wavelength multiplexing can be combined with operation of several detectors at different detection wavelength, with multi-wavelength detection [51], and with fluorescence lifetime imaging [19, 22], see Sect. 1.4.5.3.

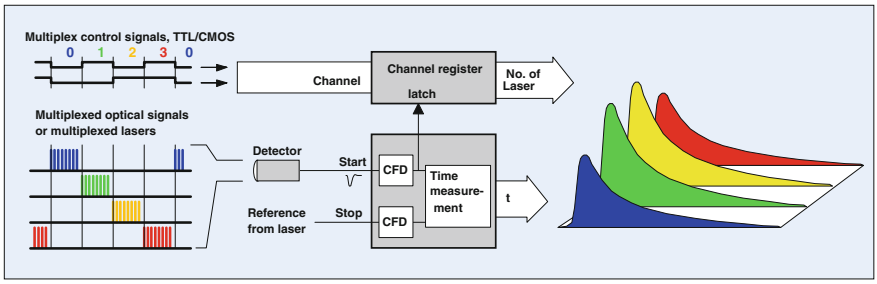

Fig. 1.16 Multiplexed TCSPC operation. Several signals are actively multiplexed into the detector, or several lasers are periodically switched. The destination in the TCSPC memory is controlled by a multiplexing signal at the 'channel' input

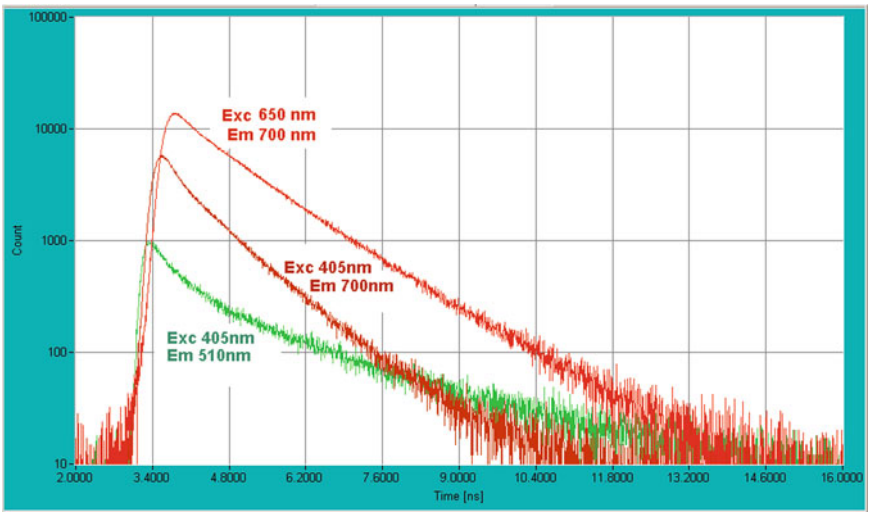

Fig. 1.17 Laser wavelength multiplexing. *Left* Fluorescence decay of a plant leaf, multiplexed excitation at 405 and 650 nm. Detection by two detectors at 510 and 700 nm

An example is shown in Fig. 1.17. A leaf was excited by two multiplexed diode lasers of 405 and 650 nm wavelength. Fluorescence was detected by two detectors at 510 and 700 nm and recorded in one TCSPC module via a router. The result are three fluorescence decay curves for different combination of excitation and emission wavelength: 405/510, 405/700, and 650/700 nm. The forth combination (650/510 nm, not shown) does not contain photons because the detection wavelength is shorter than the excitation wavelength.

It should be noted here that multiplexing of lasers can also be obtained by 'pulse-interleaved excitation', or PIE, see Sect. 1.4.5.3. In that case the lasers are multiplexed pulse by pulse. The multiplexing technique shown in Fig. 1.16 has, however, a few advantages. The most important one is that it is free of crosstalk.

The tail of the fluorescence decay excited by one laser does not show up in the decay curve excited by the next one. Moreover, there is no mutual influence of the signals via pile-up or counting-loss effects [22].

1.4.3 Spatial Multiplexing

The multiplexing technique shown in Fig. 1.16 is also used to multiplex spatial excitation or detection locations at a sample. This principle is commonly used in diffuse optical imaging of the human brain, see Fig. 1.18. A number of source fibres and detection fibres is attached to the head. The injection of the laser(s) into the source fibres is controlled by a fibre switch. The controller of the fibre switch switches though subsequent source positions and sends a status signal to the TCSPC module(s) indicating the current source position. This signal is used as a multiplexing (or routing) signal in the TCSPC modules(s) to build up separate time-of-flight distributions or fluorescence decay curves for the different source positions. The multiplexing of the source position can be combined with multiplexing of several lasers. Because diffuse-optical imaging works at high count rates the signals from the different detection positions are usually detected by individual detectors and recorded by separate TCSPC modules.

To increase the number of detector positions the setup can be extended by routers. Up to 32 detectors have been used which were connected to four TCSPC channels via four routers [48, 49].

The setup is mainly used for dynamic brain imaging, i.e. for recording relative changes in the concentration of oxy- and deoxyhemoglobin. In this case, the TCSPC systems records a time series of data, see section below. The fibre switch period is on the order of 10 ms, and the time per step of the time series is between 50 ms and a few seconds. Please see Chap. 17 of this book.

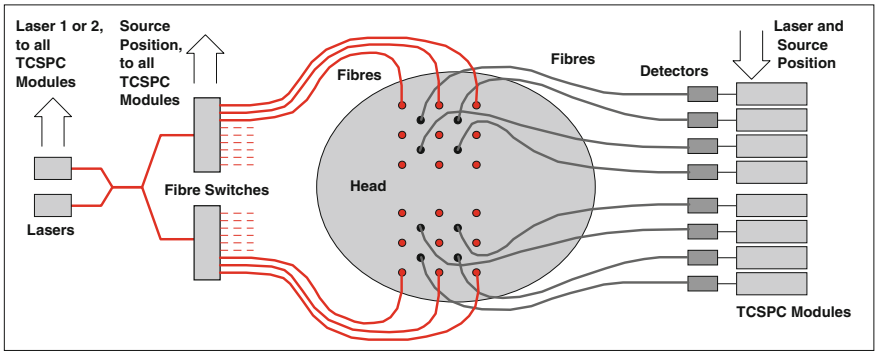

Fig. 1.18 Architecture of the 8-channel parallel DOT system described in [76]

1.4.4 Time-Series Recording

When a time-series of TCSPC data is to be recorded the first idea of classic-TCSPC users is normally to run a record-and-save procedure. The measurement would be run for a defined acquisition time, the data be read from the TCSPC device, and saved into a data file by the associated system computer. This procedure would be continued until the desired number of time steps have been performed. A procedure like this has the charm that the number of time steps is virtually unlimited. However, it has also disadvantages. An obvious one is that the speed of the sequence is limited by readout and save times. Another one is that the signal-to noise ratio of the subsequent recordings depends on the speed of the sequence. It is therefore difficult, if not impossible, to record transient changes in the recorded waveforms at millisecond or microsecond resolution.

The limitations of the record-and-save procedure can be avoided by multi-dimensional recording. The principle is shown in Fig. 1.19. The memory of the TCSPC device has space for a large number of waveforms. The number of the waveform block into which the photons are recorded is controlled by the sequencer logics of the TCSPC device. The recording starts with a user command or with an external trigger. The sequencer starts recording into the first waveform block, and then switches through the blocks in regular intervals of time.

At first glance, the principle shown in Fig. 1.19 may look like a record-and-save procedure. It is, however, different in that it records subsequent waveforms into *one single photon distribution*. There is no time needed to read and save the data. More importantly, the complete distribution can be accumulated: The experiment, e.g. the induction of a change in the fluorescence decay of a sample would be repeated, the run of the sequencer through the waveform blocks triggered by the stimulation, and the photons accumulated into a distribution according to their times after the excitation pulse and their times after the stimulation. This way, the available speed of the sequence gets entirely decoupled from the photon detection rate. It does no longer depend on the time of the individual steps of the sequence but only on the

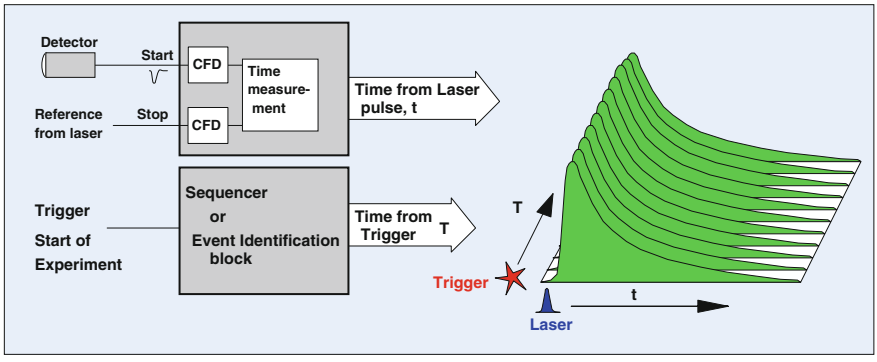

Fig. 1.19 Time-series recording

total acquisition time. The procedure even works if the sequence is so fast that only one (or less than one) photon is recorded per step. The recording would just be continued until all time channels of all waveform blocks have been filled with a reasonable amount of photons.

An example is shown in Fig. 1.20. A change in the lifetime of chlorophyll in a plant [69] was initiated by turning on the excitation light. The recording procedure steps through the curves at a rate of 50 µs/curve. Within this time, about 50 photons are recorded. To obtain a reasonable signal-to-noise ratio the procedure was repeated and the photons accumulated. The result has a high signal-to-noise ratio, despite of the short time per curve.

The procedure shown above does, of course, not require that the data in each step of the time series are only a single waveform. The data can be multi-dimensional themselves. The steps of the sequence can contain multi-wavelength data, data recorded with laser multiplexing, or combinations of both. Time-series recording can even be combined with imaging, see Sect. 1.4.5.4, and Chap. 2, Sect. 2.4.4.

Time-Series With Memory Swapping

Modern TCSPC modules have space for hundreds if not thousands of waveforms in their internal memories. A time series recorded by the principle shown in Fig. 1.19 can have a correspondingly large number of steps. However, there are applications which require to record a time-series with step times in the millisecond range over a period of time that can reach hours. Such data can be recorded by a memory swapping procedure.

The principle is shown in Fig. 1.21. The memory of the TCSPC device is split in two independent memory banks. When the measurement is started the sequencer starts to record in the first waveform block of the first bank. After a defined acquisition time it switches to the next waveform block until all blocks of the

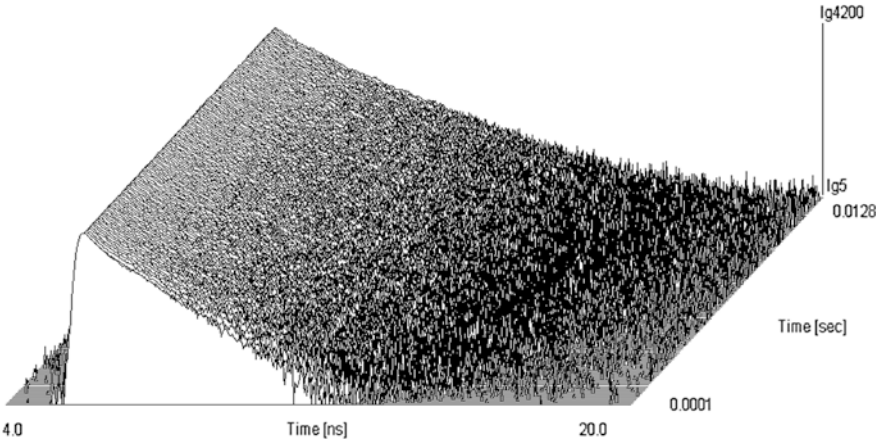

Fig. 1.20 Photochemical transient of chlorophyll in a live plant. Time per curve 100 µs, 10,000 on/off cycles were accumulated. Time-series starts from the front

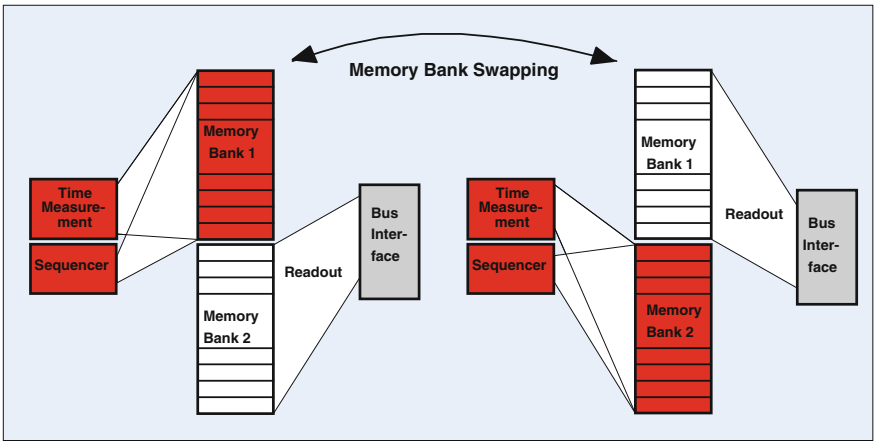

Fig. 1.21 Unlimited sequential recording by memory bank swapping. When one memory bank is full, the sequencer swaps the banks. While the sequencer writes into one bank, the other bank is read by the computer

memory bank are filled with data. Then the memory banks are swapped, and the recording continues in the other memory bank. During the time the second bank is filled with photons the system computer reads the data from the first bank and saves them into a file. This way, a virtually unlimited sequence of waveforms can be recorded without time gaps between the recordings. Also here, it is not required that a single waveform data block contains only a single waveform. The data in the subsequent blocks can be multi-wavelength data, laser multiplexing data, combinations of such data, or even FLIM data.

The memory swapping technique (or 'continuous flow mode') was originally developed for DNA analysis and single-molecule detection in a capillary gel electrophoresis setup [12]. It has been used in conjunction with TCSPC FLIM to record fast time series of chlorophyll transients [79]. It is commonly used for dynamic brain imaging by diffuse optical tomography (DOT) techniques [76, 105–108, 111, 122], see Chaps. 17 and 18 of this book. The memory swapping technique can be used with a trigger signal that starts either the recording of each bank or the recording of each data block within the current bank. It is also possible to run triggered accumulation within one memory bank, and, after a defined number of accumulations, pass to the next bank. With these options, the Continuous Flow mode provides fast and efficient recording procedures for a large number of complex experiments.

1.4.5 Fluorescence Lifetime Imaging (FLIM)

The general architecture of a TCSPC FLIM system is shown in Fig. 1.22. A laser scanning microscope (or another scanning device) scans the sample with a focused

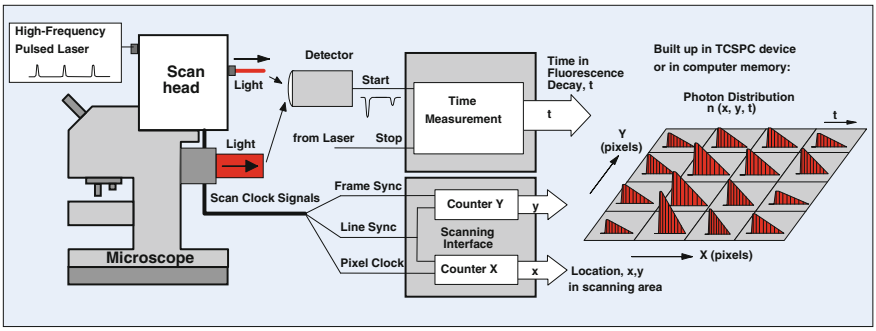

Fig. 1.22 Multidimensional TCSPC architecture for FLIM

beam of a high-repetition-rate pulsed laser. Depending on the laser used, the fluorescence in the sample can either be excited by one-photon or by multiphoton excitation. The TCSPC detector is attached either to a confocal or non-descanned port of the scanning microscope, see Chap. 2, Sect. 2.2. For every detected photon the detector sends an electrical pulse into the TCSPC module. From this pulse, the TCSPC module determines the time, t, of the photon within the laser pulse sequence (i.e. in the fluorescence decay). Moreover, the TCSPC module receives scan clock signals (pixel, line, and frame clock) from the scan controller of the microscope. A system of counters (the scanning interface) counts the pixels within each line and the lines within each frame. The counter outputs deliver the position of the laser beam, x and y in the scan area.

The information, t, x, y, is used to address a memory in which the detection events are accumulated. Thus, in the memory the distribution of the photon density over x, y, and t builds up. The result is a data array representing the pixel array of the scan, with every pixel containing a large number of time channels with photon numbers for consecutive times after the excitation pulse. In other words, the result is an image that contains a fluorescence decay curve in each pixel [13, 14, 17, 19, 22].

The procedure described above does not require that the laser beam stays at the same position until enough photons have been acquired in the decay curve of the corresponding pixel. It is only necessary that the *total pixel time*, over a large number of subsequent frames, is large enough to record a reasonable number of photons per pixel. In other words, the signal-to-noise ratio depends on the total acquisition time, not on the san rate. Thus, TCSPC FLIM works even at the highest scan rates available in laser scanning microscopes. At pixel rates used in practice, the recording process is more or less random: A photon is just stored in a memory location according to its time in the fluorescence decay and the position of the laser spot in the moment of detection.

In early TCSPC FLIM systems the photon distribution was built up directly in the hardware of the TCSPC module (see Fig. 1.11, left). The advantage of hardware accumulation is that the acquisition runs independently of the computer. It can

therefore be used at extremely high photon rates and scan speeds. The disadvantage is that the available memory space is limited. A typical application of hardware-accumulation is the 'Preview' mode of FLIM systems where images must be recordable up to almost any count rate and displayed at high image rate, but with a relatively moderate number of pixels and time channels.

The way to record larger images is to use software accumulation, i.e. the configuration shown in Fig. 1.11, right. The TCSPC device transfers the data of the individual photons and the clock pulses to the computer, and the photon distribution is built up by software. The required hardware architecture and suitable acquisition modes were available even in early TCSPC modules [22, 121]. However, the bus transfer speed and the processing capabilities of the PCs of the 1990s were insufficient for this kind of operation. At count rates above 100 kHz and pixel rates on the order of 1 MHz, as they are routinely used in FLIM, the computer was not able to read the data from the SPC module and simultaneously process them to build up a photon distribution.

The situation changed with the introduction of fast multi-core PCs. The tasks of data transfer and data processing could now be shared between the CPU cores. Count rate in the parameter-tag mode was no longer a problem. Modern TCSPC FLIM system therefore use almost exclusively software accumulation. Typical images sizes with 32-bit operating systems were 512 × 512 pixels, with 256 time channels per pixel [22]. With the introduction of Windows 7, 64 bit, and corresponding 64-bit data acquisition software, the maximum image size increased to 2048 × 2048 pixels × 256 time channels and more [139]. Pixel numbers this large are enough to record images of the maximum field of view even of the best microscope lenses. 64-bit FLIM applications are therefore rarely limited by memory size.

FLIM results are normally displayed as pseudo-colour images. The brightness represents the number of photons per pixel. The colour can be assigned to any parameter of the decay profile: The lifetime of a single-exponential approximation of the decay, the average lifetime of a multi-exponential decay, the lifetime or amplitude of a decay component, or the ratio of such parameters [22]. An example is shown in Fig. 1.23. The colour shows the amplitude-weighted mean lifetime of a double-exponential decay. The image format is 512 × 512 pixels, every pixel contains 256 time channels. Decay curves in two selected pixels are shown on the right. Similar curves are contained in any pixel of the image.

FLIM systems of the architecture shown in Fig. 1.22 are used for a wide range of applications. An overview is given in Chap. 3 of this book. The applications can essentially be divided into three classes: Measurement of parameters of the local molecular environment of the fluorophores (Chaps. 4 and 5), protein interaction experiments by FRET (Förster Energy Transfer, Chaps. 7 and 8), and imaging of metabolic parameters via the fluorescence lifetimes of endogenous fluorophores (Chaps. 13, 14, and 15). Examples for the three classes of applications are shown in Figs. 1.24 and 1.25.

Measurements of molecular environment parameters are based on changes in the fluorescence lifetime of a fluorophore with its molecular environment [92]. A commonly know effect is fluorescence quenching: The fluorescence lifetime is

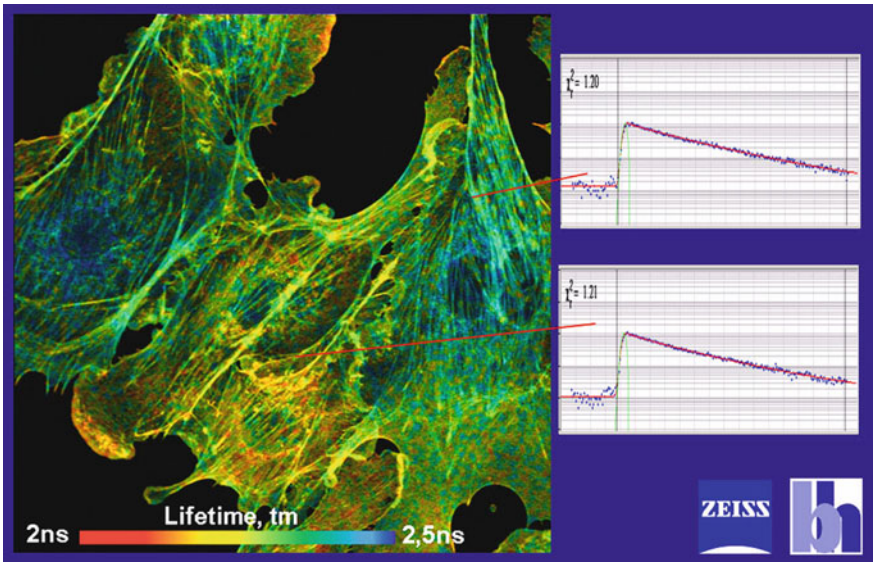

Fig. 1.23 Lifetime image of a BPAE cell, stained with Alexa 488. FLIM data 512 × 512 pixels, 256 time channels per pixel. Fluorescence decay shown for two selected pixels. Zeiss LSM 710 Intune system with Becker & Hickl Simple-Tau 150 FLIM system

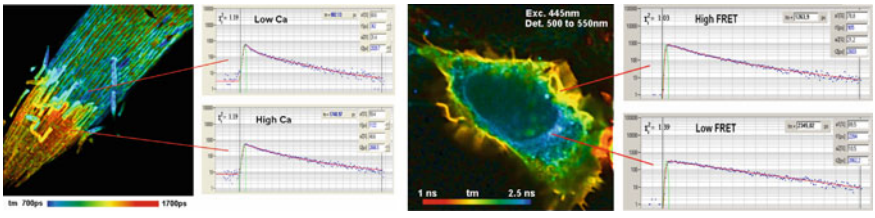

Fig. 1.24 *Left* Barley root tip, stained with *Oregon green*. Courtesy of Feifei Wang, Zhonghua Chen and Anya Salih, University of Confocal Bioimaging Facility, University of Western Sydney, Australia. Leica SP5 MP with bh SPC-150 FLIM module. *Right* Cell containing a expressing a GFP fusion protein (donor) and Cy3-labelled antibody (acceptor). Donor image, amplitude-weighted lifetime of double-exponential decay model. Zeiss LSM 710 microscope with Becker & Hickl Simple-Tau 152 FLIM system

proportional to the reciprocal concentration of the quencher, and can thus be used as a probe function for the concentration of the quencher [65, 68, 77]. A fluorophore may also have two forms of different fluorescence quantum efficiency and thus different fluorescence lifetimes. The concentration ratio of the forms, and thus the average fluorescence lifetime, may depend on the environment. Examples are Ca^{2+} sensors [88, 90, 92, 112] and pH sensors [73, 130]. There are also effects of local viscosity [89], local refractive index [143], proximity to nanoparticles and metal

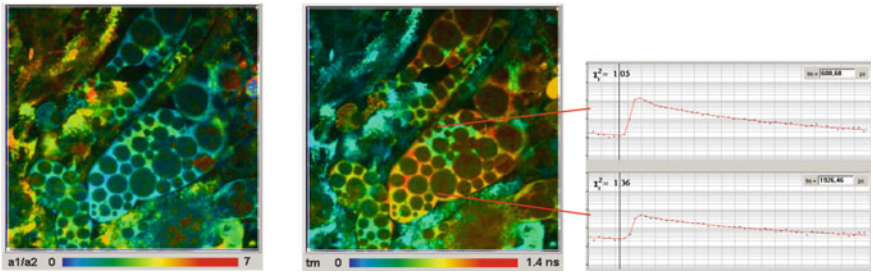

Fig. 1.25 FLIM of human salivary gland stem cells. *Left* Image of amplitude ratio, a1/a2, of fast and slow decay component. *Middle* Image of amplitude-weighted lifetime, tm. *Right* Decay curves in indicated pixels of image. Data courtesy of Aisada Uchugonova and Karsten König, Saarland University, Saarbrücken

surfaces [66, 109, 113, 124], and aggregation of the fluorophore [80]. Please see also [24, 26, 125], and Chap. 3 of this book.

The most frequent FLIM application is probably Förster resonance energy transfer (FRET), see Chaps. 7 and 8 of this book. FRET experiments use the fact that energy can be transferred from a donor to an acceptor molecule if the donor emission spectrum overlaps the acceptor excitation spectrum [63, 64]. A condition for FRET to occur is that the distance between donor and acceptor is on the order of a few nm or less. FRET is therefore used as an indicator for protein interaction. The advantage of FLIM-based FRET experiments is that the FRET efficiency is obtained from a single fluorescence-lifetime image of the donor. The problems of steady-state FRET measurements, such as directly excited acceptor fluorescence, extension of the donor emission in the acceptor channel, and unknown concentration ratio, are therefore avoided. Moreover, multi-exponential decay analysis can be used to separate the interacting donor fraction from the non-interacting one [17, 22]. There are hundreds of FRET papers based on TCSPC FLIM. An overview on the FLIM FRET applications and the corresponding literature has been given in [19, 22]. Please see also Chaps. 3, 7, and 8.

The third class of FLIM applications is the extraction of metabolic parameters from the lifetimes of endogenous fluorophores. Most autofluorescence FLIM applications use the fact that that the fluorescence lifetimes of NADH and FAD depend on the binding to proteins [91, 119]. Bound and unbound fractions can therefore be distinguised by double-exponential decay analysis and characterised by the amplitudes and lifetimes of the decay components. The ratio of bound and unbound NADH depends on the metabolic state [29, 40, 42, 56, 67, 137, 138]. FLIM data of NADH and FAD are therefore used to detect precancerous and cancerous alterations [32, 78, 95, 128, 137, 138]. It has also been shown that the fluorescence decay parameters of the NADH fluorescence change with maturation of the cells, during apoptosis and necrosis, and in response to treatment with cancer drugs [67, 86, 131, 146–148]. Autofluorescence FLIM is closely related to clinical applications [59, 84, 85, 134–136]. Please see Chaps. 13, 14 and 15 of this book.

1.4.5.1 FLIM in Parallel TCSPC Channels

A TCSPC FLIM system with a single detector detecting in a single wavelength interval can be used for a wide range of applications, see examples above. The reason that FLIM at a single wavelength works so well is that the fluorescence lifetime is inherently 'ratiometric'. The fluorescence lifetime can be considered an intensity ratio in two time intervals of the decay curve. The result thus does not depend on the concentration of the fluorophore.

The situation changes if several fluorophores with different lifetimes and different emission spectra are involved, or if fluorescence anisotropy decay data are to be recorded. Images then have to be recorded simultaneously in different wavelength intervals, or under 0° and 90° angles of polarisation. Early TCSPC FLIM systems used routing to record these signals. Modern systems more and more use fully parallel TCSPC channels.

The advantage of the parallel architecture is that the maximum count rate is higher, and that the channels are fully independent. Even if one channel saturates or a detector shuts down by overload the other channel(s) may still record correct data. Systems with two channels are standard [6, 7, 22], systems with four channels are easily possible [18], and systems with 8 parallel SPC-150 channels have been demonstrated [21, 22]. FLIM data obtained by this system are shown in Fig. 1.26.

1.4.5.2 Multi-wavelength FLIM

Multi-wavelength FLIM (also called Multi-Spectral FLIM or spectral lifetime imaging, SLIM) uses a combination of the basic FLIM technique shown in Fig. 1.22 and the multi-wavelength detection technique shown in Fig. 1.14.

The architecture of multi-wavelength FLIM is shown in Fig. 1.27. A spectrum of the fluorescence light is spread over an array of detector channels. For every photon, the time in the laser pulse period, the wavelength-channel number in the detector array, and the position, x, and y, of the laser spot in the scan area are determined. These pieces of information are used to build up a photon distribution

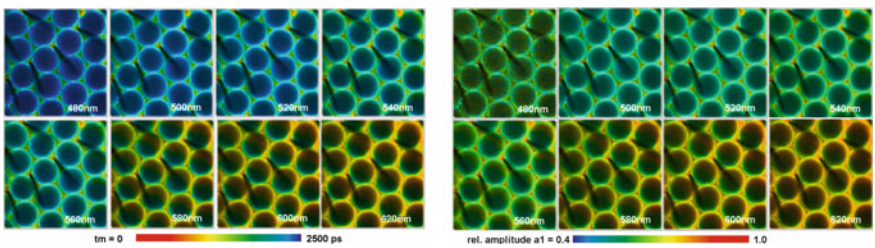

Fig. 1.26 Eight-channel parallel FLIM of a drosophila eye. Autofluorescence. Excitation at 407 nm, detection wavelength from 480 to 620 nm. *Left* Mean Lifetime of double-exponential decay. *Right* Relative amplitude of fast decay component. bh DCS-120 confocal scanning system

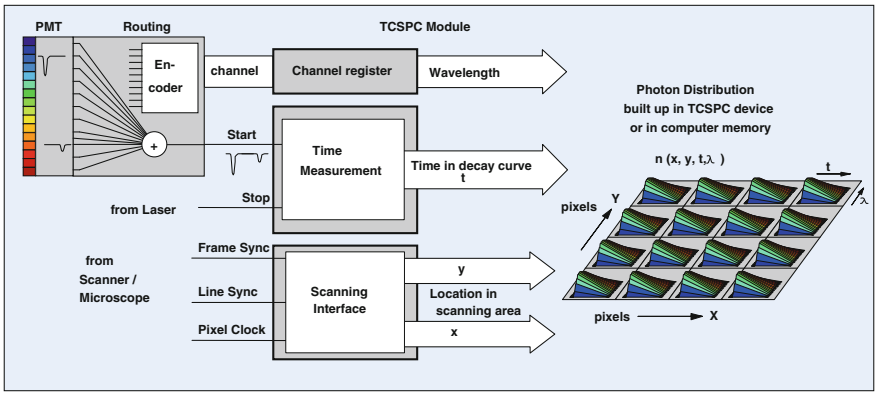

Fig. 1.27 Principle of multi-wavelength TCSPC FLIM

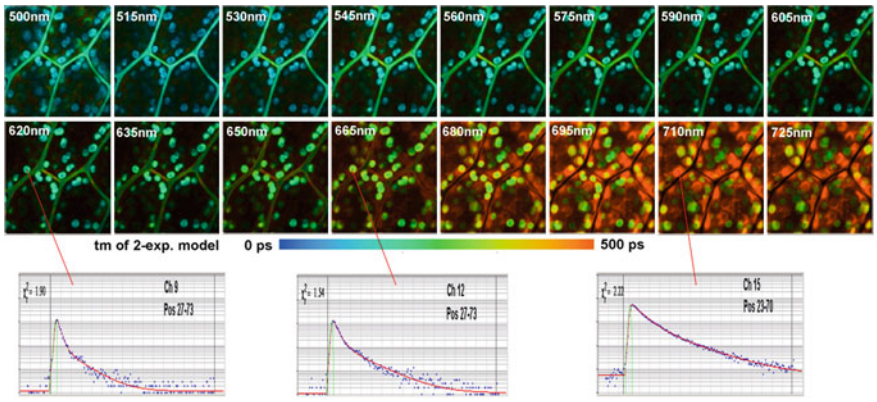

Fig. 1.28 *Top* Multi-wavelength FLIM of plant tissue, 16 wavelength intervals, 128 × 128 pixels, 256 time channels. Amplitude-weighted lifetime of double-exponential fit, normalised intensity. *Bottom* Decay curves in selected pixels of 620, 656, and 710 nm images. Two-photon excitation at 850 nm, detection from 500 to 725 nm. Zeiss LSM 710, bh Simple-Tau 150 FLIM system [7]

over the arrival times of the photons in the fluorescence decay, the wavelength, and the coordinates of the image [15, 19, 20, 22].

As for single-wavelength FLIM, the result of the recording process is an array of pixels. However, the pixels of multi-wavelength FLIM contain several decay curves for different wavelength. Each decay curve contains a large number of time channels; the time channels contain photon numbers for consecutive times after the excitation pulse. Multi-wavelength FLIM data can also be considered a set of lifetime images for different wavelength. A result of a multi-wavelength FLIM measurement is shown in Fig. 1.28.

Multi-wavelength FLIM requires a large amount of memory: For the data shown in Fig. 1.28 memory space must be provided for 16 images, each with

128 × 128 pixels, and 265 time channels per pixel. Multi-wavelength FLIM can therefore performed at reasonable pixel numbers only by building up the photon distribution in the computer memory. A significant progress has been made with the introduction of 64 bit software. In the 64-bit environment, data with 16 wavelength channels can be resolved into images of 512 × 512 pixels, and 256 time channels [139]. This is about the maximum resolution achieved for a single FLIM image in a 32 bit environment. Examples are shown in Chap. 2, Figs. 2.25 and 2.26, and in Chap. 3, Fig. 3.17.

Multi-wavelength FLIM is predominately used in applications where fluorescence signals of several fluorophores are present, and the emission of the fluorophores cannot cleanly separated by filters, or there are just too many fluorophores to get them separated by filters and dichroic beamsplitters.

Multi-wavelength FLIM was first demonstrated in 2002 by Becker et al. for recording decay data in the complete donor-acceptor wavelength range of a FRET experiment [20]. Bird et al. demonstrated the technique for lifetime imaging of stained kidney tissue samples [28]. Rück et al. used of multi-wavelength FLIM for monitoring the conversion of photosensitisers for PDT and the generation of photoproducts [126, 127]. FRET measurements by multi-wavelength FLIM were described in [30, 31, 76].

The majority of multi-wavelength FLIM applications are in autofluorescence imaging, especially imaging of the coenzymes NADH and FAD [42, 98, 128, 150]. Chorvatova and Chorvat worked out spectral unmixing techniques based on multi-wavelength FLIM data and used them to determine metabolic parameters in cardiomyocytes [40–46] and investigate their response to drugs and stress conditions.

Li et al. used multi-wavelength FLIM for NADH imaging. They found different bound/unbound ratios (represented by the a_1/a_2 ratio of the amplitudes of the lifetime components) in the cytosol and in the mitochondria, and changes induced by variable concentration of deoxyglucose [98]. They also found changes in the bound/unbound ratio when cells were exposed to sub-lethal concentrations of cadmium [99, 150].

Using two-photon excitation and multi-wavelength FLIM Li et al. were able to detect and characterise two-photon excited fluorescence from haemoglobin [154]. Multi-wavelength FLIM was used to discriminate the haemoglobin fluorescence from fluorescence of other endogenous fluorophores. This way, haemoglobin fluorescence was used for label-free imaging of microvasculature in live tissue [103, 104].

A multiphoton multi-colour excitation system with a Titanium Sapphire laser, super-continuum-generation in a photonic crystal fibre and a Becker & Hickl PML-16/SPC-150 multi-wavelength FLIM system has been developed by Li et al. [100]. The system excites tryptophane and NADH simultaneously and separates the fluorescence of both compounds spectrally. The authors found that the ratio of NADH and Tryptophane fluorescence is a sensitive indicator of cell metabolism. The same instrument was used to record Tryptophane, and NADH lifetime images in combination with SHG images in different depth of epithelial tissue [101] and for investigation of squamous intraepithelial neoplasia [81]. Simultaneous recording

of tryptophane, SHG, NADH intensity images by the system has been described in [141]. Other applications are autofluorescence lifetime imaging of leukocytes [152], multi-modal label-free imaging of zebra fish [102], and skeletal muscle tissue [141].

Multi-wavelength FLIM in combination with multiphoton tomography of human skin [84, 85, 125] was used by Dimitrow et al. [55]. The authors found changes in the fluorescence spectra and shorter fluorescence lifetime in malignant melanoma compared to normal skin.

1.4.5.3 FLIM with Excitation Wavelength Multiplexing

FLIM can be combined with excitation wavelength multiplexing. The general principle of multiplexed TCSPC is shown in Fig. 1.16. The extension of the principle to FLIM is shown in Fig. 1.29. Excitation at different wavelength is achieved by multiplexing (on/off switching) of several lasers, or by switching the wavelength of the acousto-optical filter (AOTF) of a super-continuum laser. A multiplexing signal that indicates which laser (or laser wavelength) is active is fed into the routing input of the TCSPC module. The signal represents the excitation wavelength. The TCSPC module is running the normal FLIM acquisition process: It builds up a photon distribution over the coordinates of the scan area, the photon times, and the excitation wavelength. The result is a data set that contains images for the individual excitation wavelengths. (It can also be interpreted as a single image that has several decay curves for different excitation wavelengths in its pixels.)

Different combinations of excitation and emission wavelengths can be obtained by using several detectors and a router. Modern implementations normally use several parallel TCSPC modules.

To avoid interference of the multiplexing frequency with the pixel, line, or frame frequency of the scanner multiplexing is normally synchronised with the pixels, the lines, or the frames of the scan. Details of the optical system are described in Chap. 2, Sect. 2.2.7. An typical result is shown in Fig. 1.30.

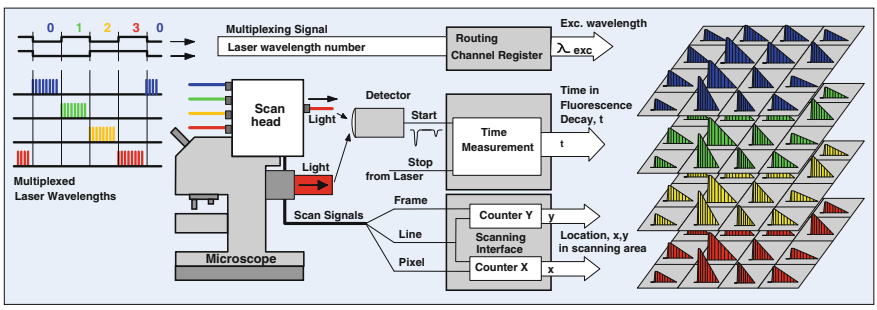

Fig. 1.29 FLIM with laser wavelength multiplexing

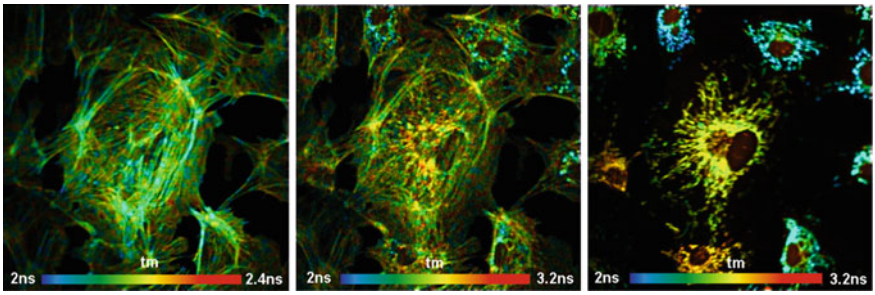

Fig. 1.30 FLIM by wavelength multiplexing, Supercontinuum laser with AOTF, two parallel SPC-150 TCSPC modules. *Left to right* Excitation 500 nm emission 525 ± 50 nm, excitation 500 nm emission 620 ± 30 nm, excitation 580 nm emission 620 ± 30 nm. 256 × 256 pixels, 256 time channels, frame-by-frame multiplexing

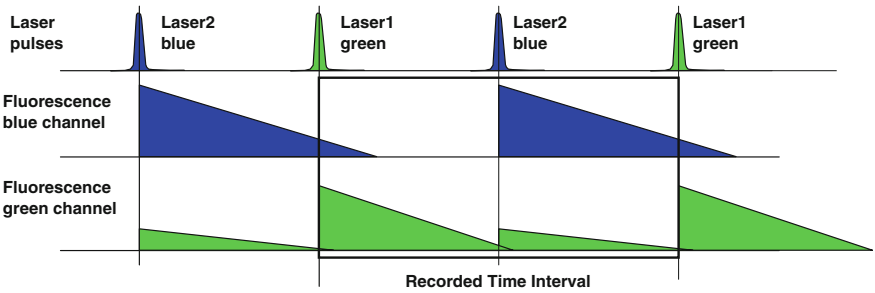

Fig. 1.31 Principle of laser wavelength multiplexing by pulse-interleaved excitation

A similar effect can be obtained by 'Pulse-Interleaved Excitation', or 'PIE'. PIE does not use the laser wavelength as a dimension of the photon distribution. Instead, the pulse trains of several (usually two) lasers are interleaved pulse by pulse, and the fluorescence decay functions excited by both lasers are recorded into a single waveform, see Fig. 1.31. The recorded waveform contains the fluorescence decay excited by one laser followed by the decay excited by the other. The data of the two excitation channels are selected by time-gating in the data analysis. Data for different combinations of excitation and emission wavelengths are recorded by using several parallel TCSPC channels or a single TCSPC channel with a router. A typical result is shown in Fig. 1.32.

The advantage of PIE in FLIM applications is that it is also applicable to lasers that cannot be on-off modulated at high speed. The disadvantage is that PIE is not entirely free of crosstalk. The tails of the fluorescence decay excited by one laser may extend into the decay excited by the other. Moreover, there is intensity crosstalk due to counting loss, and mutual influence by detector afterpulsing. Please see [22] for a comparison of PIE and laser multiplexing.

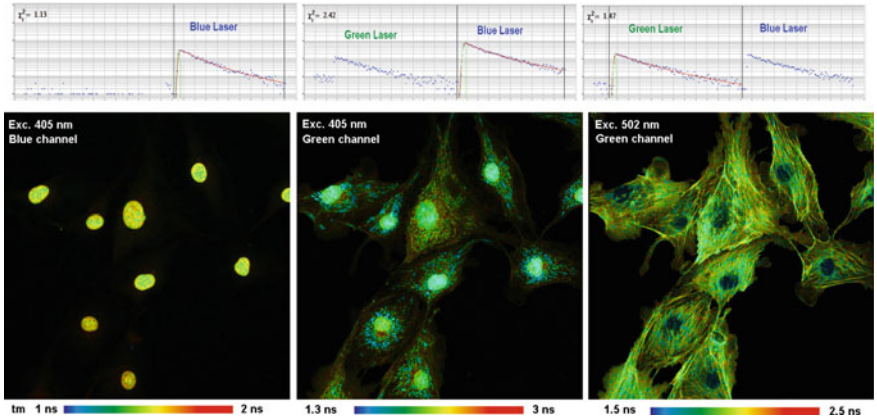

Fig. 1.32 FLIM by PIE. Zeiss LSM 710 Intune laser (*green laser*) and 405 nm ps diode laser (*blue laser*). Images recorded by two parallel SPC-150 TCSPC modules. *Left* Blue laser, blue detection channel. *Middle* Blue laser, green detection channel. *Right* Green laser, green detection channel. *Top* Decay curves in selected pixels. *Bottom* FLIM images, analysed by SPCImage, amplitude-weighted lifetime of double-exponential decay fit, time-gated intensity

1.4.5.4 FLIM Time-Series Recording

A time-series of FLIM images can be recorded by a simple record-and-save procedure. A FLIM image is recorded for a defined acquisition time or for a number of frames of the scan, and saved to a file. The procedure is repeated until the desired number of images—or steps of the time series—have been acquired [19]. The procedure is simple and has the advantage that it does not require more memory space for the photon distribution than a single FLIM recording. The disadvantage is that the save operation takes time: At least one frame of the scan is lost during the time the data are saved. A continuous sequence can be recorded by dual-memory recording [19, 22, 79]. Memory blocks are provided for two photon distributions, and the FLIM system records into one block while the data from the other one are saved. However, the time per step cannot be made faster than the time needed for saving, and the rate of the sequence is limited by the decrease of the signal-to-noise ratio with decreasing acquisition time per step of the sequence. The fastest image rate that can be achieved is 1–2 images per second, see Fig. 1.33.

A more efficient way of time-series FLIM has been provided by 64-bit data acquisition software [139]. In the 64-bit environment, the available amount of memory is so large that a large number of reasonable-size FLIM images can be recorded into one and the same photon distribution. The technique is derived from spatial ‘Mosaic’ or ‘Tile’ imaging. A FLIM mosaic is a data array (either one- or two-dimensional) which has space for a large number of FLIM data sets. The recording process starts to record FLIM data in the first mosaic element. After a defined number of frames of the scan it switches to the next element. Thus, all

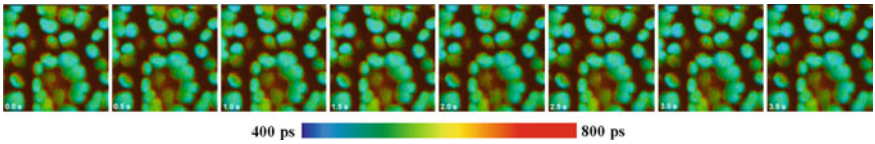

Fig. 1.33 Time series recorded at a speed of 2 images per second. Chloroplasts in a moss leaf. Dual-memory recording, images 128 × 128 pixels

elements of the mosaic are filled with data one after another. The time per element is determined by the frame time, and by the number of frames per element.

Mosaic time series recording has two advantages over the conventional record-and-save procedure. First, the transition from one mosaic element to the next occurs instantaneously. There are no time gaps between the steps of the sequence. Therefore, very fast time series can be recorded. Second, mosaic time series data can be accumulated: A lifetime change in a sample would be stimulated periodically, and the start of the mosaic recording be triggered by the stimulation. With every new stimulation the recording procedure runs through all elements of the mosaic, and accumulates the photons. Accumulation allows data to be recorded without the need of trading photon number and lifetime accuracy against the speed of the time series: The signal-to noise-ratio depends on the total acquisition time, not on the speed of the sequence. Please see Chap. 2, Sect. 2.4, Mosaic FLIM.

1.4.6 FLITS

By the technique described above a FLIM time series can be recorded down to the frame time of a fast optical scanner. Faster effects can be resolved by a combination of TCSPC and line scanning. The technique has been named 'FLITS', fluorescence *lifetime-transient* scanning [22, 23, 25]. FLITS is based on building up a photon distribution over the distance along the line of the scan, the experiment time after a stimulation of the sample, and the arrival times of the photons after the excitation pulses. The principle is shown in Fig. 1.34.

FLITS uses the same recording procedure as FLIM. Similar as for FLIM, the result is an array of pixels, each of which contains a fluorescence decay curve in form of photon numbers in subsequent time channels. The recoding is synchronised with the scan by pixel clock pulses (which indicate the transition to the next pixel of the line) and line clock pulses, which indicate the transition from the end of the line back to the start. The procedure differs from FLIM in that the frame clock pulses does not come from the scanner but from an external event that stimulates a fluorescence-lifetime change in the sample. The TCSPC module thus records a photon distribution which has the Y coordinate of FLIM replaced with a coordinate that represents how often the scanner scanned along the line since the stimulation. In other words, the Y coordinate is the time after the stimulation given in multiples of the line time.

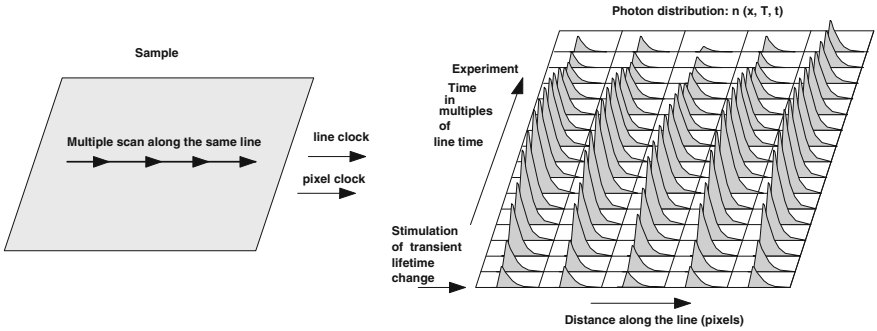

Fig. 1.34 Principle of FLITS. A sample is scanned along a line. The TCSPC system builds up a photon distribution over the distance along the line, the time after a stimulation of the sample, and the times of the photons after the excitation pulses

As long as the stimulation occurs only once the recording process is simple: The sequencer of the TCSPC module [19, 22] starts to run with the stimulation, and puts the photons in consecutive experiment-time channels along the T axis.

A FLITS recording is shown in Fig. 1.35, left. It shows the non-photochemical lifetime transient of chlorophyll [69] recorded after the start of illumination. The horizontal axis is the distance along the line scanned, the vertical axis (bottom to top) is the experiment time, T, in this case the time from the start of the illumination. Decay curves for a selected pixel within the line are shown for T = 0.5, 7.5, and 13.4 s.

The result shown in Fig. 1.35, left, is identical with a time-series of line scans. However, there is an important difference: The data are still in the memory (either in the on-board memory of the TCSPC module or in the computer) when the sequence is completed. Thus, the recording process can be made repetitive: The sample would be stimulated periodically, and the start of T triggered by the stimulation. The recording then runs along the T axis periodically, and the photons are accumulated into one and the same photon distribution.

With repetitive stimulation of the sample, it is no longer necessary that each T step acquires enough photons to obtain a complete decay curve in each pixel and T channel. No matter when and from where a photon arrives, it is assigned to the right location in x, the right experiment time, T, and to the right arrival time, t, after the laser pulse. As in the case of FLIM, a desired signal-to-noise-ratio is obtained by simply running the recording process for a sufficiently long acquisition time. Obviously, the resolution in T is limited by the period of the line scan only, which is about 1 ms for the commonly used galvanometer scanners. For resonance scanners and polygon scanners (see Chap. 2) the line time can be made even shorter.

An example of an accumulated FLITS recording is shown in Fig. 1.35 right. It shows the photochemical transient [69] of the chlorophyll in a plant. The result was obtained by turning on and off the laser periodically, and recording the photons by

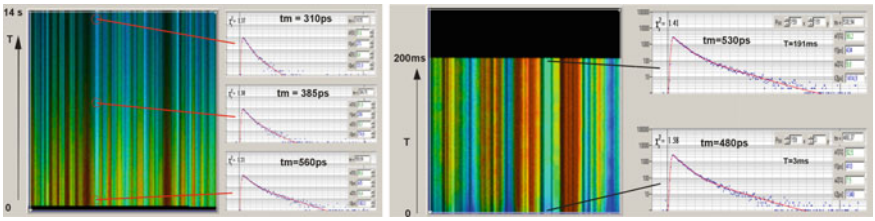

Fig. 1.35 FLITs recordings of chlorophyll transients. *Left* Non-photochemical transient, vertical time scale 0–14 s, decay curves shown for a selected pixel at T = 0.5, 7.5, and 13.4 s after turn-on of the laser. *Right* Photochemical transient. Vertical time scale 0–200 ms, decay curves shown for a selected pixel at T = 3 and 191 ms into the laser-on phases. The amplitude-weighted lifetime increases from 480 to 530 ps

triggered accumulation. The T scale is from 0 to 200 ms. Decay curves are shown for a selected pixel within the line for T = 3 and 191 ms into the laser-on phases. The amplitude-weighted lifetime increases from 480 to 530 ps.

The application of FLITS to Ca^{2+} imaging in neurons is described in Chap. 5 of this book.

1.4.7 Phosphorescence Lifetime Imaging (PLIM)

Phosphorescence occurs when an excited molecule transits from the first excited singlet state, S1, into the first triplet state, T1, and returns from there to the ground state by emitting a photon [92]. Both the S1-T1 transition and the T1-S0 transition are 'forbidden' processes. The transition rates are therefore much smaller than for the S1-S0 transition. That means that phosphorescence is a slow process, with lifetimes on the order of microseconds or even milliseconds. The usual approach to phosphorescence recording is to reduce the excitation pulse rate and extend the time scale of decay recording to microseconds or milliseconds. Except for fluorophores of high intersystem crossing rate, the results obtained this way are disappointing.

There are several reasons why simply decreasing the repetition rate does not work well. Both are related to the low S1-T1 transition rate. The excitation energy injected into the molecules is preferentially dissipated by the S1-S0 transition, and not deposited in the T1 state. The T1 population therefore remains low, and so does the phosphorescence intensity. Simply increasing the peak power of the excitation pulse meets technical constraints, or causes nonlinear effects in the sample. The second problem is that high excitation peak power also causes high peak intensity of fluorescence. The fluorescence pulse not only leads to the detection of one or several photons per excitation pulse and thus violates the rules of TCSPC detection. It can become so strong that it causes temporary overload in the detector.

These problems can be solved by exciting phosphorescence with laser pulses longer than the fluorescence lifetime. The long pulse width increases the population of the triplet state without increasing the peak fluorescence intensity. Similarly,

a group of laser pulses instead of a single pulse can be used. The principle is shown in Fig. 1.36.

A high-frequency pulsed laser is modulated on/off at a period several times longer than the phosphorescence lifetime. The laser pulses within the 'on' phase of the modulation period excite fluorescence and build up phosphorescence. The 'off' phase contains only phosphorescence. The advantage of this excitation principle is not only that it can be used for multi-photon excitation but also that it can be used *to record fluorescence and phosphorescence decay data simultaneously*. This is achieved by assigning two times to every photon, one of which is the time in the laser pulse period, t, the other the time in the laser modulation period, T. Two separate photon distributions are built up, one over t, the other over T. The distribution over t is the fluorescence decay, the distribution over T the phosphorescence decay. The principle can be used both for single-curve recording and for lifetime imaging [22].

The architecture of a combined FLIM and PLIM system is shown in Fig. 1.37. The TCSPC module works in the parameter-tag mode. The times of the photons, t,

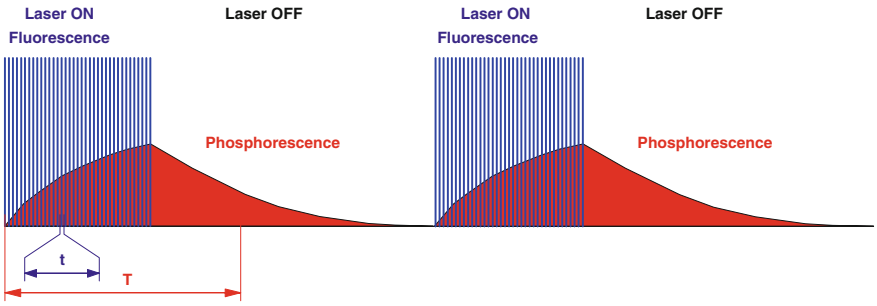

Fig. 1.36 Excitation principle for combined FLIM/PLIM

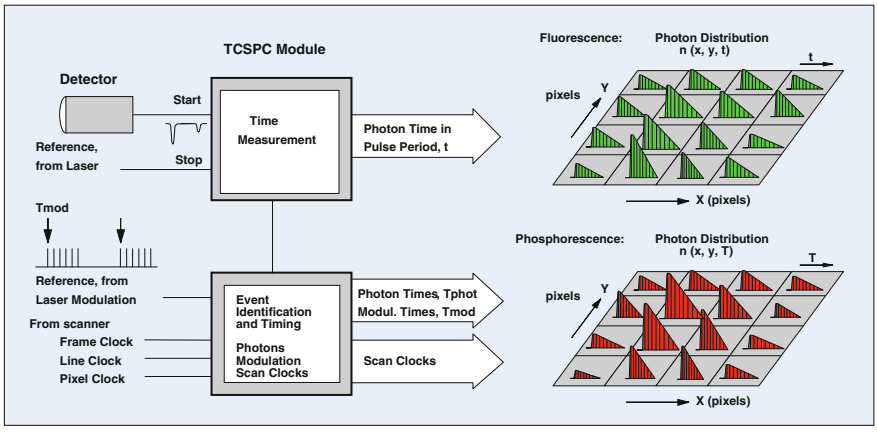

Fig. 1.37 Combined FLIM/PLIM system

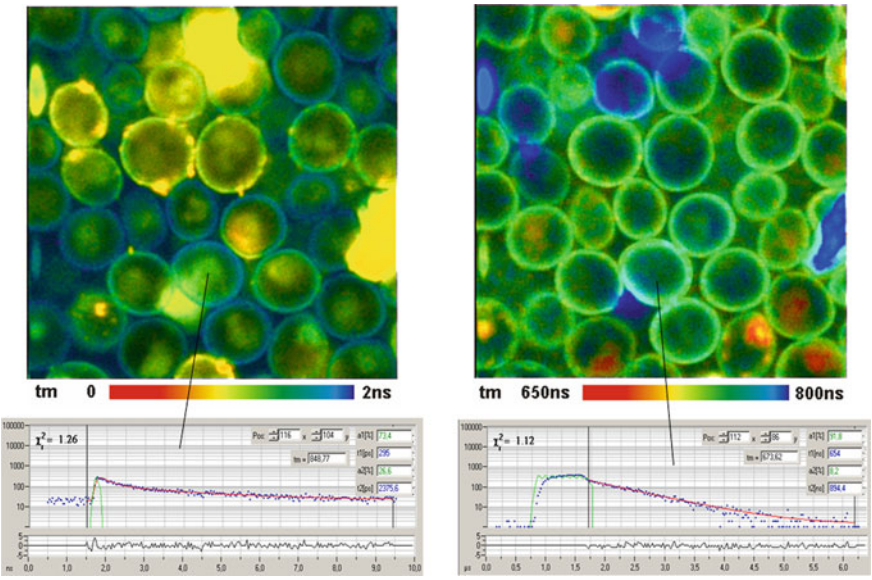

Fig. 1.38 Combined FLIM/PLIM recording. Yeast cells stained with a ruthenium dye. FLIM (*left*) shows autofluorescence, PLIM (*right*) phosphorescence of the Ruthenium dye

within the laser pulse period are measured by the normal time-measurement block. The 'Event Identification' block (see Fig. 1.11 right) determines absolute times, T_{phot}, of the photons. Moreover, it receives a reference signal from the laser modulation and clock pulses from the scanner. From these signals, it determines absolute times for the modulation reference, T_{mod}, and for the scan clocks, T_{pixel}, T_{line}, and T_{frame}. The values are put in a data stream together with the photon data. From these data, the computer software determines the locations, x, y, of the individual photons in the scan area, and the times of the photons within the modulation period, $T = T_{phot} - T_{mod.}$ The software builds up two photon distributions, one over the scan coordinates and the times, t, and another over the scan coordinates and the times, T. The first one is a fluorescence lifetime image during the on-phase of the laser modulation period, the second one a phosphorescence lifetime image.

An example of a FLIM/PLIM measurement is shown in Fig. 1.38. The figure shows yeast cells stained with tris (2,2′-bipyridyl) dichlororuthenium (II) hexahydrate. The FLIM image is shown Fig. 1.38, left. It is dominated by autofluorescence of the cells. PLIM is shown in Fig. 1.38, right. The phosphorescence comes from the ruthenium dye. Decay curves in selected pixels are shown at the bottom. The time scale of FLIM is 0–10 ns, the time scale of PLIM 0–6.5 µs.

PLIM applications aim at suppression of autofluorescence [4, 5], and, more importantly, oxygen-concentration sensing. Phosphorescence from almost any phosphorescing compound is strongly quenched by oxygen. The phosphorescence

lifetime can therefore be used to determine oxygen concentrations [53, 54, 129]. Combined FLIM/PLIM is especially promising because it is able to record metabolic information via FLIM while monitoring the oxygen concentration via PLIM. Please see Chap. 6 of this book.

1.4.8 Multi-dimensional Recording by Modulation of Experiment Parameters

The lifetime imaging techniques described above scan the spatial location of the fluorescence excitation and detection and record the shape of the optical signal as a function of the scan coordinates. There are other TCSPC applications that aim on recording optical signals as functions of parameters which are not necessarily spatial ones. The task can be solved in a similar way as FLIM: Parameters in the sample or in the experiment setup are modulated, the TCSPC process is synchronised with the parameter modulation via scan clock pulses, and a photon distribution is recorded over the parameters and the time in the optical signal. A typical experiment of this class is used in plasma physics for the investigation of barrier discharges.

Barrier discharges occur if the electric field between two isolator-coated electrodes exceeds a critical value, see Fig. 1.39. The visible discharge phenomenon consists of a large number of micro-discharges with nanosecond duration and kHz frequency.

Barrier discharges are technically highly relevant: They are a degradation mechanism of insulators in electrical systems, and they are used in a wide variety of plasma applications, e.g. for cleanup of exhaust gases. The investigation of the discharges is difficult: They occur at random times, the duration of the light pulses is on the order of a few nanoseconds, and the intensity is low. Ideally, it would be desirable to record the shapes of the optical pulses as a function of the gap voltage and the distance along the gap for selectable wavelength. Exactly this task can be solved by multi-dimensional TCSPC. The principal setup is shown in Fig. 1.40.

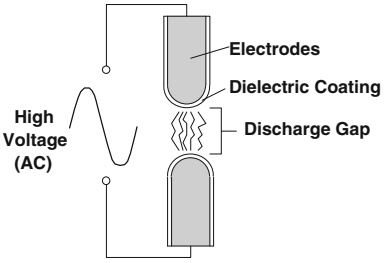

Fig. 1.39 Barrier discharge between dielectrically coated electrodes

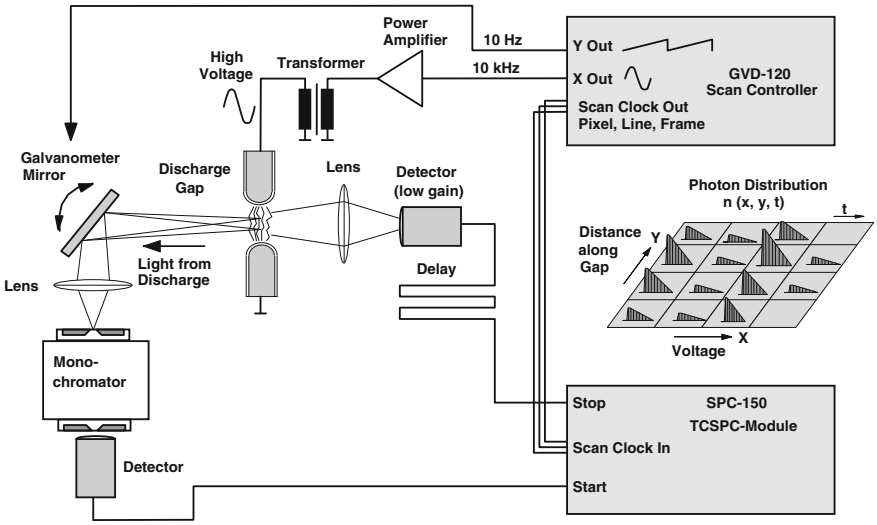

Fig. 1.40 Principle of the setup for barrier discharge measurements

One output of a digital signal synthesizer (in the present case a bh GVD-120 scan controller) delivers a sinusoidal output voltage. The voltage is amplified, transformed to a voltage in the 10 kV range, and applied across the discharge gap. A second output of the synthesizer (the Y output of the scan controller) drives a galvanometer mirror. The galvanometer mirror periodically scans the spot from which the light is detected along the discharge gap. A monochromator selects the desired detection wavelength. Single photons of the selected signal are detected by a PMT module. The photon pulses are connected to the start input of an SPC-150 TCSPC module.

The stop input for the TCSPC module comes from a second PMT. This PMT detects light from the entire discharge gap in a wide spectral range. For every discharge, it detects about 1000 photons. Operated at a relatively low gain, it delivers a timing reference for the TCSPC module. The recording process is synchronised with the operation of the scan controller via scan clock pulses. Consequently, the TCSPC module records a photon distribution over the phase of the gap voltage (X), the distance along the discharge gap (Y), and the times of the photons in the optical pulses generated by the discharges.

Figure 1.41, shows the waveform of the optical pulses as a function of the distance over the gap integrated over the positive and the negative half-waves of the gap voltage. It can be seen that the optical pulse varies along the gap. It also differs between the positive and the negative half-wave of the gap voltage.

Figure 1.42 shows the intensity over the time in the optical pulse and the distance along the gap for four different phases in the gap voltage, Fig. 1.43 the intensity over the time in the pulse and the phase in the gap voltage for four subsequent distance intervals along the gap. The images reveal a complex

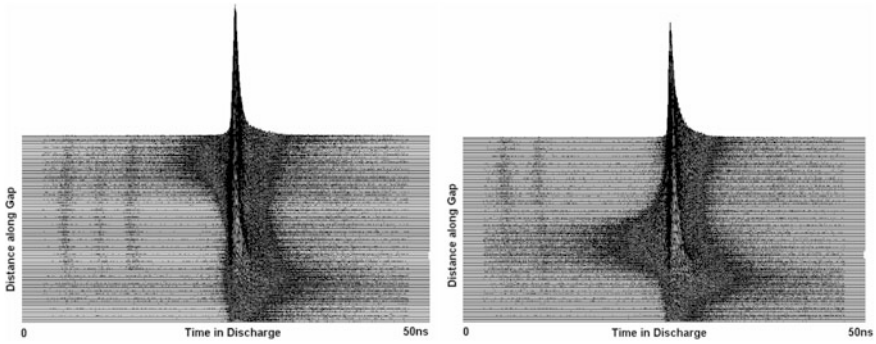

Fig. 1.41 Waveform of optical pulses for different distance along the gap for positive (*left*) and negative (*right*) half-wave of the gap voltage. Data courtesy of Ronny Brandenburg, INP Greifswald, Germany

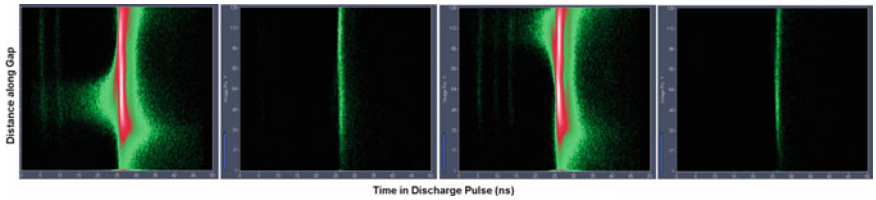

Fig. 1.42 Intensity over time in discharge pulse and distance along the gap for four subsequent phase intervals (*quarter waves*) in the gap voltage. Horizontal scale 0–50 ns. Data courtesy of Ronny Brandenburg, INP Greifswald, Germany

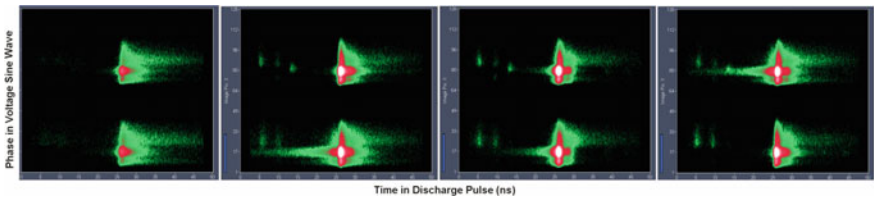

Fig. 1.43 Intensity over time in the discharge pulse and phase in the gap voltage for four subsequent distance intervals along the gap. Horizontal scale 0–50 ns. Data courtesy of Ronny Brandenburg, INP Greifswald, Germany

behaviour of the light pulses. The shape varies both with the location in the gap and with the gap voltage at which the discharges occur. There are also pre-pulses that occur some 10 ns before the main pulse.

Similar as the other multi-dimensional TCSPC applications, the principle shown above has no inherent limitation of the rate at which an experiment parameter is modulated. This is very important for barrier-discharge measurements: The

frequency of the gap voltage must be in the 10 kHz range, and matched to the resonance frequency of the transformer-gap combination. Sequential recording of the voltage-dependence—e.g. by keeping the voltage constant until enough discharges have occurred and enough photons been recorded—is therefore not an option.

Barrier-discharge systems exist in several variants. Some are using sub-sets of the principle shown above, e.g. point measurements at selected location in the gap, or slow scanning along the gap distance. However, all are using the phase of the gap voltage as a parameter of a multi-dimensional TCSPC process. Please see [37, 38, 71, 74, 75, 82, 87, 145] for technical details and for results.

1.5 Using Parameter-Tagged Single-Photon Data

The techniques described above transfer parameter-tagged single-photon data into the system computer and build up photon distributions by software. Once a photon has been put into the photon distribution the information associated to it is no longer needed and, normally, discarded.

Parameter-tagged photon data may, however, be used to build up other results than multi-dimensional photon distributions. When the data are recorded it may even not be clear how exactly they are to be processed. User-interaction during the data processing may be required, or the processing may be so time-consuming that it cannot be performed online. In these cases the single photon data may be saved for later off-line processing. The general structure of parameter-tagged single-photon data and the use of such data in a few typical applications will be described below.

1.5.1 Structure of Parameter-Tagged Single-Photon Data

Parameter-tagged single-photon data contain information about the individual photons detected by the TCSPC device [19, 22]. An example of the structure of such data is shown in Fig. 1.44.

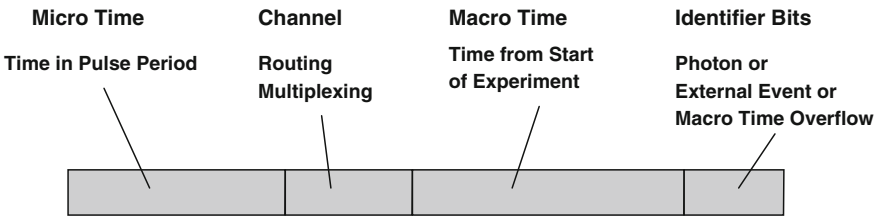

Fig. 1.44 Structure of parameter-tagged data

Each photon is tagged with its time after the excitation pulse (the 'micro time'), the time from the start of the recording (the 'macro time'), and the data word from the 'channel' register of the TCSPC device. External events, such as transitions of scan clock signals, are also put in the stream of parameter-tagged data. Several identifier bits mark a particular entry either as a photon or as an external event. Of course, the entries of external events do not contain valid micro time information. The micro time bits of external events may therefore be used to transfer other information.

The macro-time clock has normally a resolution of on the order of few 10 ns. However, an experiment can be run over a time of seconds, minutes, or even hours. Because the number of macro time bits in the photon data words is limited the macro time will overflow in regular intervals during the recording. To allow the data processing software to account for the overflows these are marked in the data. Macro time overflows can either be attached to the photon data words or be put in the data stream the same way as external events.

1.5.2 Calculation of FCS from Parameter-Tagged Data

Fluorescence Correlation Spectroscopy is based on recording fluorescence from a limited number of fluorescing molecules in a small sample volume, and correlating intensity fluctuations caused by the motion of the molecules [123]. The data processing procedure for FCS is usually described by the correlation functions

$$G(\tau) = \lim_{T\to\infty} \frac{1}{2T} \int_{-T}^{+T} I(t)I(t+\tau)dt \quad G_{12}(\tau) = \lim_{T\to\infty} \frac{1}{2T} \int_{-T}^{+T} I_1(t)I_2(t+\tau)dt$$

where $G(\tau)$ is the autocorrelation of a single signal, $I(t)$, and $G_{12}(\tau)$ the cross-correlation function of two signals, $I_1(t)$ and $I_2(t)$.

For photon counts, N, in consecutive, discrete time channels $G(\tau)$ and $G_{12}(\tau)$ can be obtained by calculating

$$G(\tau) = \sum N(t) \cdot N(t+\tau) \quad \text{and} \quad G_{12}(\tau) = \sum N_1(t) \cdot N_2(t+\tau)$$

The general behaviour of the auto- and cross-correlation functions is illustrated in Fig. 1.45. For a randomly fluctuating signal, *I(t)*, the autocorrelation function $G(\tau)$ delivers high values only if the intensity values, I, at a given time, t, and at a later time, $t + \tau$ are correlated. Uncorrelated fluctuations of I cancel over the integration time of the experiment. Similarly, $G_{12}(\tau)$ delivers high values if the fluctuations in both signals, $I_1(t)$ and $I_2(t + \tau)$, correlate with each other. The drop of $G(\tau)$ and $G_{12}(\tau)$ over the shift time, τ, shows over which length of time the fluctuations are correlated.

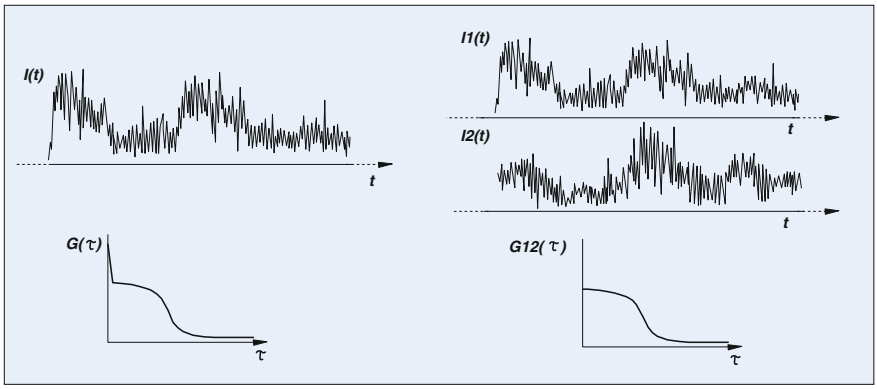

Fig. 1.45 General behaviour of the autocorrelation function, $G(\tau)$, of a signal I and the cross-correlation function, $G_{12}(\tau)$, of the signals I_1 and I_2

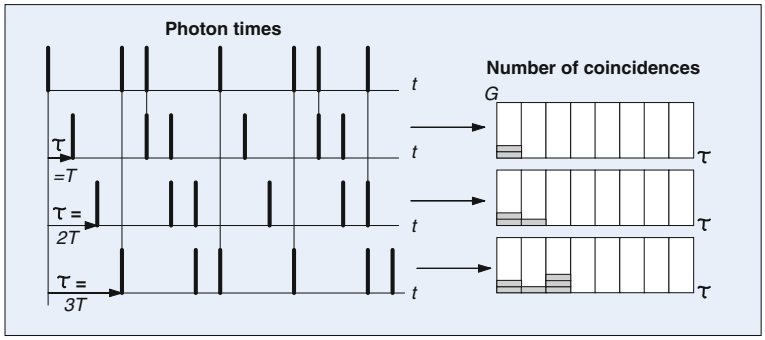

Fig. 1.46 Calculation of the autocorrelation function from TCSPC time-tag data

The equations shown above are based on the assumption that the intensity waveforms are analog signals. However, TCSPC data are not a continuous waveform as those shown in Fig. 1.45. Instead, the data describe a random sequence of individual detection events. In fact, the events can be (and usually are) so rare that there is less than one photon within the range of τ over which the intensities are to be correlated. The equations shown above are therefore inappropriate to calculate correlation functions from parameter-tagged photon data recorded by TCSPC.

The general correlation procedure for parameter-tagged photon data is illustrated in Fig. 1.46. In typical TCSPC data, the time-channel width, T, is the period of the macro-time clock. It is shorter than the dead time of the detector/photon counter combination. Therefore only one photon can be recorded in a particular macro time period. Consequently, $N(t)$ and $N(t + \tau)$ can only be 0 or 1. The calculation of the autocorrelation function therefore becomes a simple shift, compare, and histogramming procedure. The times of the individual photons are subsequently shifted

by one macro-time clock period, T, and compared with the original detection times. The coincidences found between the shifted and the unshifted data are transferred into a histogram of the number of coincidences, G, versus the shift time, τ. The obtained $G(\tau)$ is the (un-normalised) autocorrelation function.

The cross-correlation function between two signals is obtained by a similar procedure. However, the photon times of one detector channel are shifted versus the photon times of the other channel.

To obtain intensity-independent correlation curves the results of the algorithm shown in Fig. 1.46 need to be normalised. Normalisation can be considered the ratio of the number of coincidences found in the recorded signal and the number of coincidences expected for an uncorrelated signal of the same count rate. The normalised autocorrelation and cross-correlation functions are

$$G_n(\tau) = G(\tau)\ \frac{n_T}{N_P^2}$$

with n_T = total number of time intervals, Np = total number of photons, and

$$G_{12n}(\tau) = \ G_{12}(\tau)\ \frac{n_t}{N_{P1}N_{P2}}$$

with n_T = total number of time intervals, N_{p1} = total number of photons in signal 1, N_{p2} = total number of photons in signal 2.

The procedure illustrated in Fig. 1.46 yields $G(\tau)$ in equidistant τ channels. The width of the τ channels is equal to the macro time clock period of the SPC module, T. The algorithm is known as the 'Linear-Tau' algorithm. Unfortunately, for long correlation times the algorithm results in an extremely large number of τ channels in $G(\tau)$, and in intolerably long calculation times.

Therefore, the algorithm is usually modified by applying binning steps to the photon data during the correlation procedure. The procedure is illustrated in Fig. 1.47.

The procedure starts with a number of shift-and-compare steps as shown in Fig. 1.46. After a number of steps the remaining photon data are binned. Then the correlation procedure is continued on the binned data. The new time bins can contain several photons. Therefore, the photon numbers in the original and the shifted data have to be multiplied. After a number of shift steps the data are binned again, and the procedure is continued. The procedure is called 'Multi-Tau' algorithm. Despite of the binning operations, it yields shorter calculation times than the Linear-Tau algorithm. It also delivers the logarithmic τ axis commonly used for FCS curves.

The correlation procedures shown above can be used to calculate FCS curves online. In this case, photons are constantly recorded, and the data transferred into the system computer. In certain intervals, usually a few seconds, the software calculates a correlation function (or several correlation functions if several detectors are active) on the data that have arrived within this time. The coincidences for the

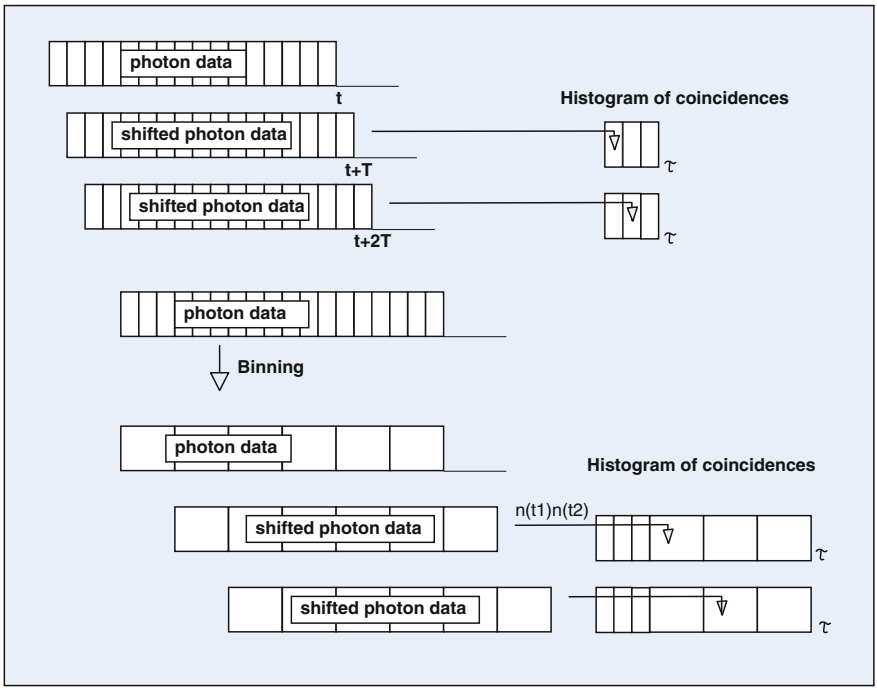

Fig. 1.47 Correlation procedure with progressive binning

subsequent intervals are summed up in a common histogram, see Figs. 1.46, and 1.47, right. Of course, the procedure requires that the recording-time intervals be longer than the maximum time, τ, over which the photons are correlated. Moreover, photons recorded in one interval must still be available in the next one to correlate late photons in one interval with early photons in the next.

An example of FCS calculation from parameter-tagged data is shown in Fig. 1.48. The data were recorded in a confocal microscope [6] from a diluted solution of fluorescein. On average, about 0.4 molecules were in the detection volume at a time. The average count rate was about 5000 photons/s.

Figure 1.48, top, shows an intensity trace of the recorded signals at time-bin width of 10 µs, and over a time interval of 10 ms. Due to the low detection rate there is no more than 1 photon per time bin, and there are about 50 photons over a period of time of 10 ms.

The autocorrelation function is shown at the bottom of Fig. 1.48. Note that the τ scale of the FCS curve is the same as the length of the time intervals of the intensity trace on the left. However, the FCS curve was calculated over the complete acquisition time of the measurement, in this case 120 s. It shows a clear correlation curve of the intensity fluctuations caused by diffusion of the molecules. That a correlation curve is obtained from the data shown in Fig. 1.48, top, may surprise at first glance. It is a result of the fact that the data have been correlated over a period of 120 s, not

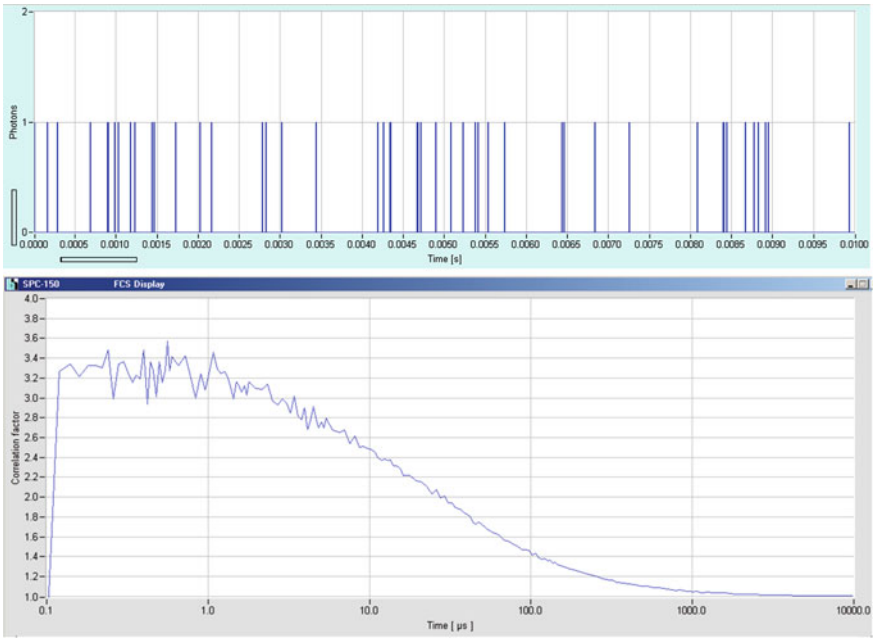

Fig. 1.48 *Top* Intensity trace, time bin width 10 µs, displayed time interval 10 ms. *Bottom* Autocorrelation curve from the same signal correlation time from 100 ns to 10 ms. Calculated over acquisition time of 120 s

only over the time intervals shown in the intensity trace in Fig. 1.48, top. This is another example that the signal-to-noise ratio in single-photon counting experiments depends on the total acquisition time, not on the time over which the photons are correlated.

Most FCS applications aim at the estimation of the size of labelled biomolecules, on the detection of interaction between biomolecules, and on the determination of the number of fluorescent molecules attached to a special biomolecule. The size of the molecules can be derived from the diffusion time, i.e. the point of the auto-correlation function at which drops to 50 % of its maximum. More accurately, the diffusion time is obtained by fitting the autocorrelation function with an appropriate model. Interaction of molecules is derived from the cross-correlation functions. Different biomolecules are labelled with fluorophores of different absorption and emission spectra. The cross-correlation (FCCS) function of the two signals indicates whether the constructs diffuse together or independently.

In terms of TCSPC, data acquisition FCS and FCCS are very simple applications. They even do not need the micro-times of the photons, and do not need a pulsed excitation source. FCS and FCCS are, however, anything but simple in respect to the optical system and the detectors: Excellent optical efficiency, low chromatic and spherical aberration, excellent alignment of the confocal optics, and excellent detection efficiency are necessary to obtain good FCS results.

The basic optical setup for a dual-colour FCS experiment is shown in Fig. 1.49. Two diode lasers are used to excite fluorescence in the sample. The sample contains two fluorophores, Atto 488 and Atto 647N, each of them excited by one of the lasers. The fluorescence is detected by two detectors through different filters. The detection (macro) times of the photons are recorded by two TCSPC channels. The photons of the channels are auto-correlated and cross-correlated by the instrument software. For the setup shown in Fig. 1.49 a bh DCS-120 confocal FLIM system was used. The principle can, however, be implemented in almost any confocal laser scanning microscope.

Auto- and cross-correlation functions of free Atto 488 and Atto 647N fluorophores are shown in Fig. 1.50, left. There is autocorrelation for the signals from both fluorophores (Red and blue curves) but no cross-correlation between the

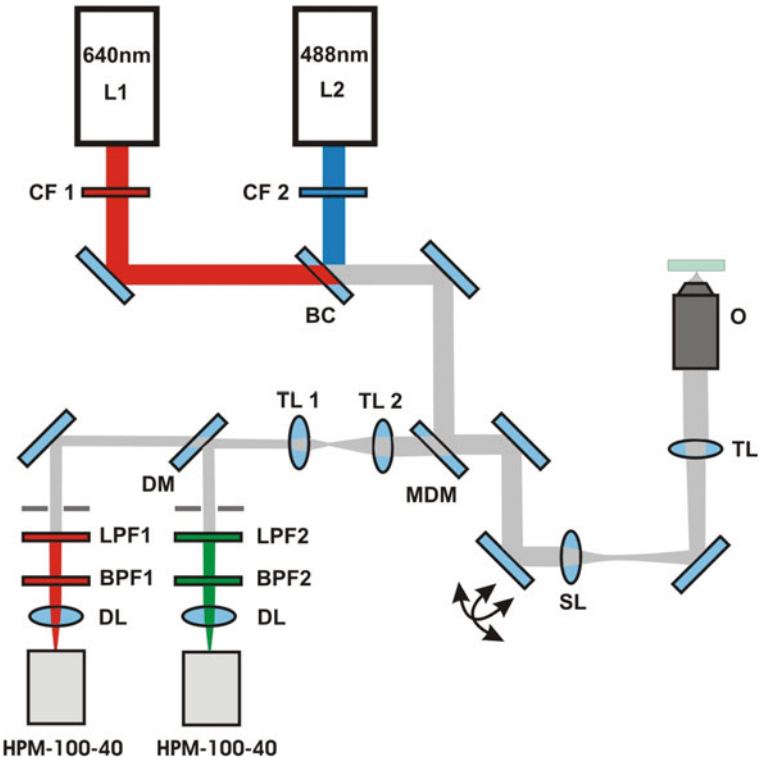

Fig. 1.49 Dual-colour FCCS setup based on BDL-SMN lasers and DSC-120 confocal FLIM system. *L1*, *L2* BDL-SMN picosecond/CW diode laser, operated in CW mode. *BC* Beam combiner. *MDM* Dual-wavelength dichroic mirror, 488/647 nm. *SL* Scan lens of DCS-120 scan head. *TL* tube lens of microscope. *O* Microscope objective lens. *TL1*, *TL2* Lenses, forming a telscope projecting the beam into comfocal pinholes. *DM* Dichroic mirror, splits the light of the two fluorophores. *LPF1*, *LPF2* Long-pass filters. *BPF1* and *BPF2* band-pass filters. *DL* Lens centering the light on the detectors

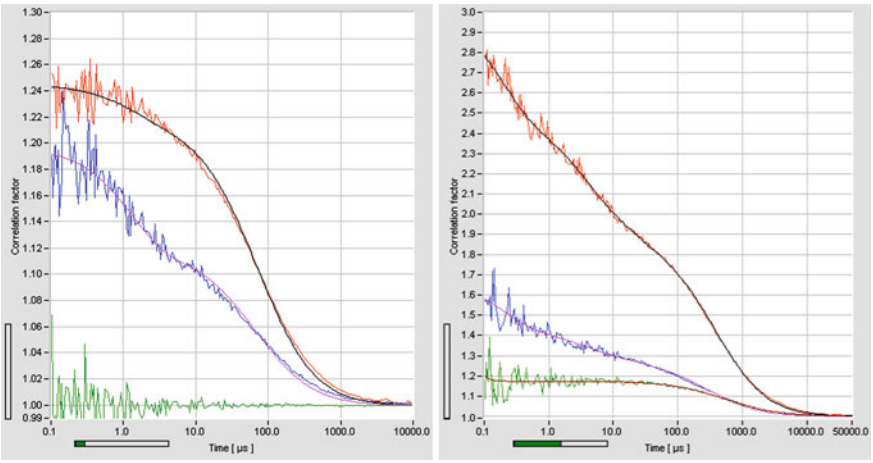

Fig. 1.50 *Left* Atto 488/7 nM Atto 647N, molecules not linked. *Right* Alexa 488 and Cy5 partially linked by double-stranded DNA. *Blue* and *Red* Autocorrelation. *Green* Cross-correlation

signals (green). Curves for a 40-base pair double-stranded DNA labelled with Alexa 488 and Cy5 are shown in Fig. 1.50, right. There is a significant cross-correlation (green curve) showing that DNA strands labelled with different fluorophores are partially linked to each other.

A third application of FCS—determination of the number of fluorophore molecules attached to a biomolecule—is used to obtain information on the structure and conformation of the molecules. Special subunits of the biomolecule are labelled by fluorescent antibodies or—more reliably—by expressing fluorescent proteins. From the amplitude of the autocorrelation function and the number of counts the brightness of the labelled biomolecule can be obtained. For a given fluorophore, this is proportional to the number of fluorophores attached to it. Provided the labelling or expression is complete it represents the number of subunits under investigation. The technique has been used to determine the structure of CaMKII by combined fluorescence anisotropy, and fluorescence correlation techniques [115].

The correlation function is also used for perfusion measurements in diffuse optical imaging. The technique is based on correlating intensity fluctuations of photons scattered in the blood flowing in the tissue [39]. The basic setup is shown in Fig. 1.51, left. A laser injects light into the tissue via a fibre. The light at a different spot is collected by another fibre and detected by a photon counting detector. An autocorrelation function of the intensity is calculated from the absolute times of the photons. To obtain a useful correlation function it is required that the laser have a coherence length longer than the average path length in the tissue, and that the fibres have diameters on the order of 20 µm or less. A correlation function recorded at a human forearm is shown in Fig. 1.51, right.

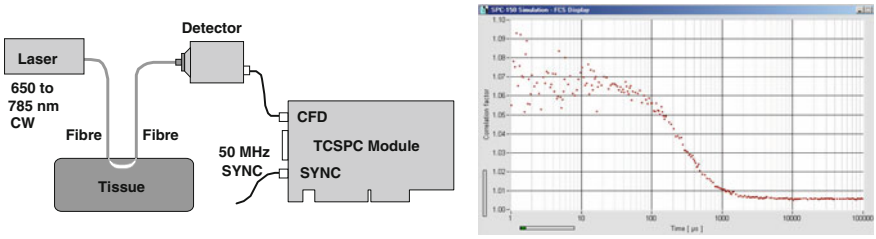

Fig. 1.51 Diffuse optical correlation. *Left* Basic experiment setup. *Right* Correlation curve recorded at a human forearm, bh SPC-150 TCSPC module

1.5.2.1 Including the Micro-Time of TCSPC in FCS

The calculation of FCS by the algorithms shown above are based exclusively on the macro times of the photons. FCS and Cross-FCS can therefore also be obtained by excitation with CW lasers. If the fluorescence is excited by pulsed lasers the micro time of the photons can be used in several ways.

Simultaneous Recording of Fluorescence Decay Functions

Obviously, fluorescence decay curves can be obtained in parallel with the FCS measurement. All that is necessary is to build up a photon distribution over the micro times of the photons. The fluorescence decay is helpful to identify problems, such as contamination by autofluorescence or Raman scattering. Fluorescence decay times can also be used to improve FCS analysis of correlation curves with several components.

Time Gating

FCS signals are sometimes contaminated by Raman scattering. Raman light shows up as a sharp peak at the beginning of the fluorescence decay. The peak can be gated off, either by setting a time gate in the TCSPC hardware [22], or by excluding photons with macro times outside a defined time window (Fig. 1.52). Time gating can also be necessary when FCS is recorded with pulse-interleaved excitation (PIE).

Filtered FCS

Micro times can be used to separate FCS signals of fluorophores of different fluorescence decay times. In that case, the photons are weighted with a coefficient derived from the micro time via a filter function [33, 62]. The technique can also be

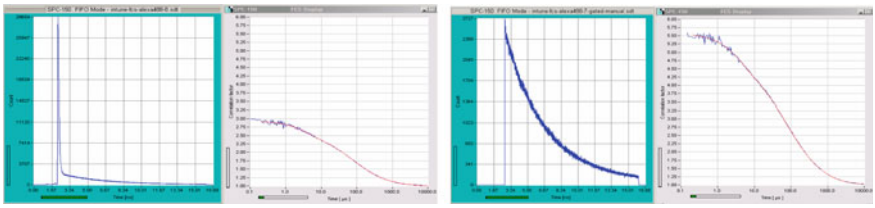

Fig. 1.52 Gated FCS, detected light contains Raman scattering. *Left* Fluorescence decay with Raman peak, FCS curve calculated from entire signal. *Right* Raman peak gated out, FCS calculated inside selected time window. Note the increased FCS amplitude. Zeiss Intune system, Becker & Hickl SPC-150 TCSPC FLIM Module with HPM-100-40 hybrid detectors

used to reject detector background signals, Raman scattering, or unwanted background fluorescence.

Global Fit of FCS and Decay Data

Another way to improve the separation of several diffusion components in FCS analysis has been developed by Anthony and Berland [2]. Assume there are several fluorescing species of similar or nearly similar excitation and emission spectra. These species diffuse at different speed. In principle, the two diffusion components can be separated by fitting the FCS data with a model that contains two diffusion components. The problem is that, unless the diffusion times are very different, the components can be separated only at limited accuracy. However, if the two species have different fluorescence lifetimes the relative amplitudes can be obtained via double-exponential decay analysis. The amplitudes can then be used in the FCS analysis to obtain a more reliable fit. An even more robust fit is obtained if all parameters, i.e. the fluorescence lifetimes, the component amplitudes, and the diffusion times of the components are determined in a global fit [2, 3].

FCS Down to the Picosecond Time Scale

By including the micro times, photons can be correlated down to the picosecond time scale. The principles has been introduced by Felekyan et al. in 2005 [60]. They used two synchronised TCSPC modules in the setup shown in Fig. 1.53, left. Fluorescence in a sample is excited by a CW laser in a femtoliter sample volume. The fluorescence light is split into two detectors, the signals of which are recorded by two TCSPC modules. The stop pulses for the time measurement come from an external 80 MHz clock generator. The internal macro time clock is synchronised to the signal at the stop inputs of the TCSPC modules [19]. The TCSPC modules work in the parameter-tag-mode; the single-photon data are constantly read by the system computer. By using both the micro times and the macro times FCS data were

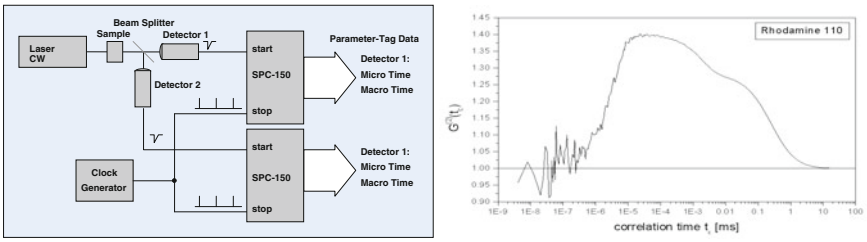

Fig. 1.53 Picosecond fluorescence correlation with two synchronised TCSPC modules

obtained at a resolution of about 20 ps. The algorithm is described in [60], and included in a single-molecule analysis software package of the University of Düsseldorf [61].

At first glance, it may look surprising that this method works: The TCSPC modules used in the setup determine the micro times by advanced TAC/ADC principles. This delivers high resolution micro times at excellent stability. However, the time scales of the micro time and the macro time are not strictly comparable, and there may be minor overlaps or gaps in the two time scales. It can also happen that photons with arrival times too close to a stop pulse are not recorded. However, all these effects are correlated to the signal from the external clock oscillator. They are *not* correlated to the photons. The correlation of the photon data therefore delivers correct results.

Applications of picosecond correlation to dye-exchange dynamics of R123 in micellar solutions and supra-molecular cyclodextrin-pyronin complexes are described in [116, 1]. Combined with FRET measurement, the method has been used to study conformational changes in a yellow chameleon Ca^{+} sensor [36]. It has also been used to study complexes of adamantane and cyclodextrin [70], and micellar exchange dynamics [35].

Picosecond correlation is easy with TCSPC devices using direct time-to-digital conversion by TDC chips, especially if the chips contain several channels operated by the same internal clock. A picosecond correlation curve recorded by a Becker & Hickl DPC-230 photon correlator is shown in Fig. 1.54.

1.5.3 Single-Molecule Burst Analysis

Consider a solution of fluorescent molecules, excited by a focused laser beam through a microscope lens, with the emitted photons being detected through a confocal pinhole that transmits light only from a volume of diffraction limited size. When the concentration of fluorescent molecules is small enough only one molecule will be in the detection volume at a time. As the molecule diffuses through the excitation/detection volume it emits photons. Thus, the detection signal consist of bursts of photons caused by individual molecules. The photon bursts can be

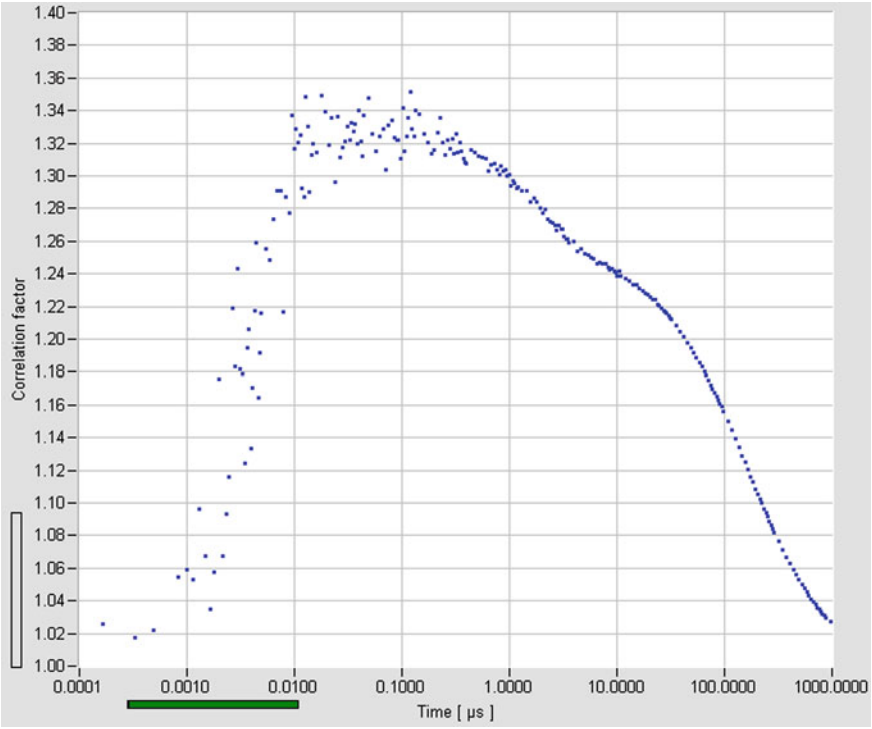

Fig. 1.54 Picosecond photon correlation by DPC-230 photon correlator

recorded in the parameter-tag mode of a TCSPC device. Photon bursts from an Alexa 488 Dextrane construct are shown in Fig. 1.55.

The idea behind single-molecule burst analysis is to determine as many as possible fluorescence parameters for the individual bursts and build up multi-dimensional histograms of the frequency of the bursts versus the parameter values. A demonstration of the technique has been given by Widengren et al. [149]. FRET pairs were constructed by linking different fluorophores to a deoxyoligonucleotide. A mixture of these constructs was investigated in a confocal optical setup. The photons were detected simultaneously under 0° and 90° polarisation and in two wavelength intervals, and recorded by TCSPC in the parameter-tag mode. Individual bursts were identified in the parameter-tag data. Within the bursts, the fluorescence intensities and the fluorescence lifetime in both wavelength channels and the fluorescence anisotropy were determined. From these data, two-dimensional histograms of the burst frequency were built up versus the intensity ratio in the two wavelength channels, the fluorescence lifetime and the fluorescence anisotropy. Donor-only constructs, donor-acceptor constructs, and donor-acceptor constructs of different donor-acceptor distance could be clearly identified in the histograms, see Fig. 1.56.

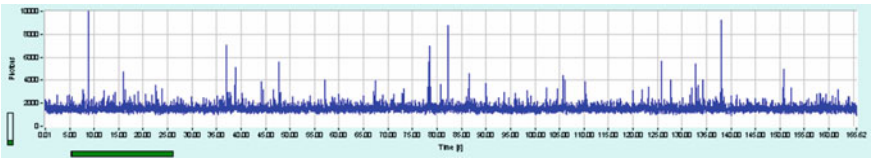

Fig. 1.55 Photon bursts from single molecules in an intensity trace calculated from parameter-tag data

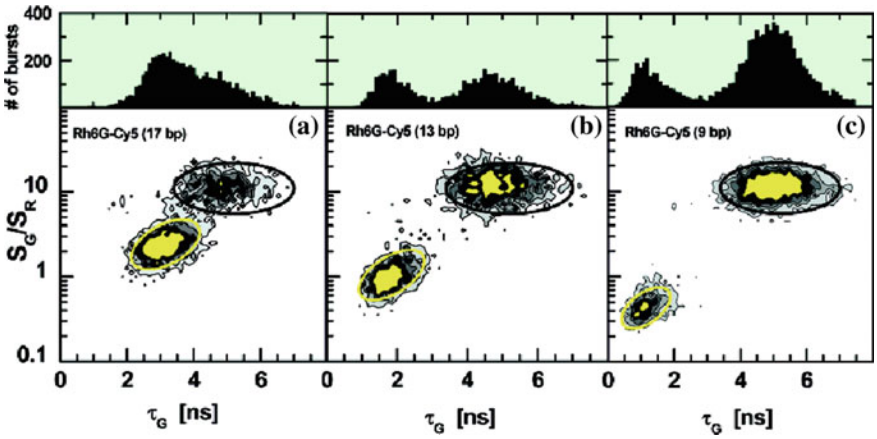

Fig. 1.56 Frequency of photon bursts in a histogram of the donor/acceptor intensity ratio versus the donor lifetime. The *black ellipses* mark donor-only events, the *yellow ellipses* donor-acceptor events. *Left to right* Donor-acceptor distance 17, 13, and 9 base pairs. With permission, from [149], by American Chemical Society

A frequent application of burst analysis is the detection of conformational changes in biomolecules by single-molecule FRET techniques. Please see Chap. 9 of this book.

The technique has been used to detect conformational changes in the sarcoendoplasmic reticulum of calcium ATPase (SERCA). Two constructs were used. One was had Cerulean at the N-terminus and an EYFP intra-sequence tag in the nucleotide-binding domain (CY-CERCA, Fig. 1.57a). The other was labelled with GFP in the N-domain and a TagRFP in the N-terminus (Fig. 1.57b). The molecules were freely diffusing through the laser focus of a Leica SP5 two-photon microscope. Fluorescence was detected simultaneously in two emission wavelength intervals corresponding to the emission spectra of Cerulean and GFP. The photons were recorded by a bh SPC-830 TCSPC module via a router. Parameter-tag data were recorded and analysed as shown in Fig. 1.57c–f.

Figure 1.57c shows the intensity bursts caused by the transition of the molecules through the laser focus. The bursts were identified in the data stream and a lifetime

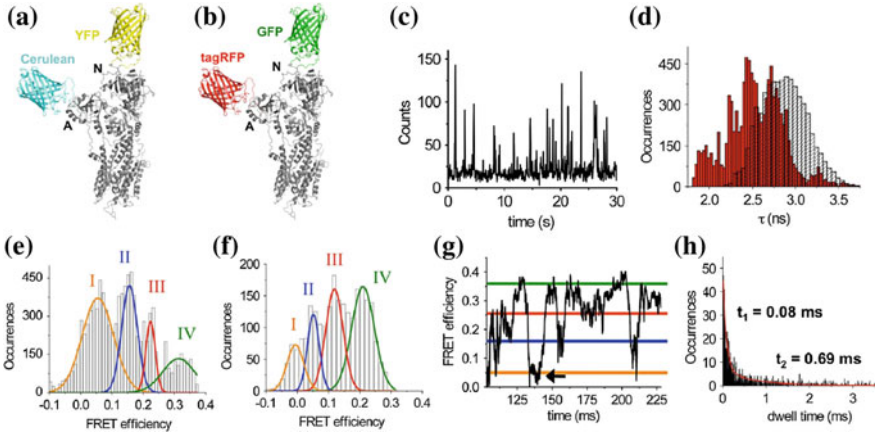

Fig. 1.57 Single-molecule FRET of SERCA. **a** CY-SERCA comprises a Cerulean FRET donor fused to the N-terminus of SERCA (*grey*) in the actuator, or A-domain, and an intrasequence FP inserted in the nucleotide-binding, or N-domain. **b** RG-SERCA is an analogous construct composed of a TagRFP acceptor fused to the N-terminus in the A-domain and GFP (*green*) donor inserted in the N-domain. **c** Time-trace of fluorescence bursts from single molecules. **d** Histogram of the fluorescence lifetimes obtained from RG-SERCA (*red*) or control GFP-SERCA (*black*). **e** Histogram of the FRET efficiency calculated from the lifetime measurements shown in panel **d.** A Gaussian fit reveals subpopulations consistent with four discrete conformations of SERCA. **f** CY-SERCA also exhibited four discrete RET states. The reduced FRET efficiency of these states (compared to panel **e**) was consistent with a larger Förster radius. **g** RG-SERCA single-molecule FRET time trajectory. The *horizontal lines* indicate States *I–IV* (*orange* through *green*) identified by Gaussian analysis of the distributions of the FRET efficiency. **h** Analysis of the dwell time for SERCA-sampling States *I–IV* revealed a biphasic distribution of dwell times characterized by fast (t_1) and slow (t_2) kinetics. With permission, from [118]

analysis performed in the individual bursts. A histogram of the lifetimes obtained over a large number of bursts is shown in Fig. 1.57d. Changes in the conformation of the molecules result in different FRET efficiency and thus in different fluorescence lifetimes. The lifetimes were therefore translated into FRET efficiencies. Histograms of the FRET efficiencies are shown in Fig. 1.57e, f. Four different FRET states are visible in the figures. The FRET efficiencies were extracted by fitting the distributions with four gaussian distributions. Figure 1.57g shows the fluctuations of the FRET efficiency within a single burst. Also here, four different FRET efficiencies can be identified. Figure 1.57h shows a distribution of the duration the molecules spent in each FRET state. The distribution was fitted with a bi-exponential model. This revealed two characteristic times, t1 and t2, the system stayed in the individual FRET states.

The experiments were extended to SERCA-expressing cultured rabbit cardio myocytes. Also here, four discrete structural states were found. The relative populations of these states oscillated with electrical pacing. Low-FRET states were

most populated in the low-Ca phase (diastole), high-FRET states correlated with high Ca (systole).

Burst recording and molecule FRET analysis has been used to detect conformational changes [52, 57] also in F_0F_1-ATP synthase and even determine the step size of its molecular rotor [58], see Chap. 9. EGFP was fused to the C terminus of subunit α, and Alexa 568 attached to residue E2C at one of the c subunits, see Fig. 1.58, left. FRET occurs between the EGFP and the Alexa 568. The entire C ring (blue) rotates against the upper part of the structure. This causes a change in the distance between the EGFP and the Alexa 568 and, consequently, a change in the FRET efficiency. The FRET efficiency was determined by recording fluorescence in a red (acceptor, Alexa) and a green (donor (EGFP)) detection channel and calculating ratios of the count numbers. Bursts from constructs containing both the donor and the acceptor were selected by wavelength-multiplexed excitation and analysing the count numbers in both channels. Intensity traces and FRET distances for two selected bursts are shown in Fig. 1.58, right.

There are two different models of the rotation of the C ring against the upper part of the structure. One model predicts a step size of the rotation of 120°, the other a step size of 36°. To decide between the two models the distances of subsequent FRET states were identified in the data. The distances for subsequent states were determined, and the density plot of distances shown in Fig. 1.59 was built up. It shows the frequency of data pairs for subsequent FRET states (one distance versus the subsequent one). The result is compatible with the prediction for 36° step size (white line) but not with 120° step size (black line). Please see Chap. 9 for more details.

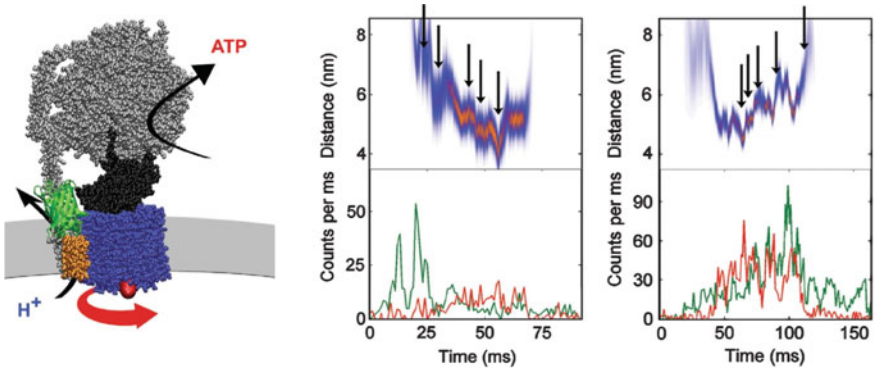

Fig. 1.58 *Left* Model of *E. coli* F0F1-ATP synthase labelled with EGFP (donor, *green*, fused to the C terminus of subunit α, *orange*) and Alexa 568 (acceptor, *red*, at residue E2C at one of the c subunits (*blue*). *Right* Counts in *green* (donor) and *red* (acceptor) detection channel (*bottom*) and donor-acceptor distances derived from FRET intensities for two selected photon bursts. The *arrows* mark steps in the FRET distance. With permission, from [58]

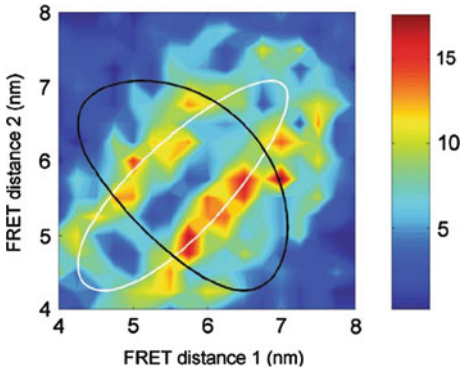

Fig. 1.59 FRET transition density plot. Distance pairs for subsequent FRET states, distance 1 and distance 2. The result is compatible with the prediction for 36° step size (*white line*) but not with 120° (*black line*). With permission, from [58]

1.6 Summary

Multi-dimensional TCSPC builds up photon distributions over various parameters of the photons. These can be inherent parameters of the photons, such as wavelength, polarisation, or the location they are coming from, parameters describing the state of the sample in the moment of the photon detection, or parameters actively varied in the experiment setup. The advantage over classic approaches is that no photons are suppressed in the recording process, and that the speed of the parameter variation gets de-coupled from the photon detection rate. The signal-to-noise rate of the results depends only on the total acquisition time, not on the time scale at which individual parameters are resolved. Typical applications of multi-dimensional TCSPC are multi-wavelength recording of fluorescence decay data, diffuse optical imaging experiments, multi-spectral lifetime imaging of biological tissue, recording of physiological changes in biological objects, fluorescence lifetime imaging (FLIM), or combinations of these techniques like multi-wavelength FLIM, excitation-wavelength multiplexed FLIM, time-series FLIM, recording of transient changes in the fluorescence of a sample along a line (FLITS) or across a selected area, and simultaneous fluorescence and phosphorescence lifetime imaging (FLIM/PLIM). Moreover, data of the individual photons can be stored and used to build up FCS and FCCS data or multi-dimensional histograms of single-molecule parameters over a longer period of time or a large number of molecules. There are possible TCSPC applications which have not finally been explored yet: TCSPC could be combined with electro-physiology, with protein folding experiments, temperature-jump techniques, and experiments that record changes in the metabolic state of cells and tissue.

References

1. W. Al-Soufi, B. Reija, M. Novo, Suren Felekyan, R. Kühnemuth, C.A.M. Seidel, Fluorescence correlation spectroscopy, a tool to investigate supramolecular dynamics: inclusion complexes of pyronines with cyclodextrin. J. Am. Chem. Soc. **127**, 8775–8784 (2005)
2. N. Anthony, K. Berland, Global Analysis in Fluorescence Correlation Spectroscopy and Fluorescence Lifetime Microscopy, in *Methods in Enzymology 518, Fluorescence Fluctuation Spectroscopy (FFS), Part A*, ed. by S.Y. Tetin (Academic Press, San Diego, 2013)
3. N.R. Anthony, K.M. Berland, Global analysis enhances resolution and sensitivity in fluorescence fluctuation measurements. PLoS ONE **9**, e90456, www.plosone.ord
4. E. Baggaley, M.R. Gill, N.H. Green, D. Turton, I.V. Sazanovich, S.W. Botchway, C. Smythe, J.W. Haycock, J.A. Weinstein, J.A. Thomas, Dinuclear Ruthenium(II) complexes as two-photon, time-resolved emission microscopy probes for cellular DNA. Angew. Chem. Int. Ed. Engl. **53**, 3367–3371 (2014)
5. E. Baggaley, S.W. Botchway, J.W. Haycock, H. Morris, I.V. Sazanovich, J.A.G. Williams, J.A. Weinstein, Long-lived metal complexes open up microsecond lifetime imaging microscopy under multiphoton excitation: from FLIM to PLIM and beyond. Chem. Sci. **5**, 879–886 (2014)
6. Becker & Hickl GmbH, DCS-120 Confocal Scanning FLIM Systems, user handbook, edition 2012, www.becker-hickl.com
7. Becker & Hickl GmbH, Modular FLIM systems for Zeiss LSM 510 and LSM 710 family laser scanning microscopes. User handbook, 5th edition. www.becker-hickl.com
8. W. Becker, H. Stiel, Verfahren zur mehrdimensionalen zeitaufgelösten Messung von Lichtsignalen durch Photonenzählung, Patent WP 282 518, G01 J/327 7903 (1998)
9. W. Becker, H. Stiel, E. Klose, Flexible Instrument for time-correlated single photon counting. Rev. Sci. Instrum. **62**, 2991–2996 (1991)
10. W. Becker, Verfahren und Vorrichtung zur zeitkorrelierten Einzelphotonenzählung mit hoher Registrierrate, Patent DE 43 39 784 (1993)
11. W. Becker, Verfahren und Vorrichtung zur Messung von Lichtsignalen mit zeitlicher und räumlicher Auflösung, Patent DE 43 39 787 (1993)
12. W. Becker, H. Hickl, C. Zander, K.H. Drexhage, M. Sauer, S. Siebert, J. Wolfrum, Time-resolved detection and identification of single analyte molecules in microcapillaries by time-correlated single photon counting. Rev. Sci. Instrum. **70**, 1835–1841 (1999)
13. W. Becker, K. Benndorf, A. Bergmann, C. Biskup, K. König, U. Tirlapur, T. Zimmer, FRET measurements by TCSPC laser scanning microscopy. Proc. SPIE **4431**, 94–98 (2001)
14. W. Becker, A. Bergmann, K. König, U. Tirlapur, Picosecond fluorescence lifetime microscopy by TCSPC imaging. Proc. SPIE **4262**, 414–419 (2001)
15. W. Becker, A. Bergmann, C. Biskup, T. Zimmer, N. Klöcker, K. Benndorf, Multi-wavelength TCSPC lifetime imaging. Proc. SPIE **4620**, 79–84 (2002)
16. W. Becker, A. Bergmann, G. Weiss, Lifetime Imaging with the Zeiss LSM-510. Proc. SPIE **4620**, 30–35 (2002)
17. W. Becker, A. Bergmann, M.A. Hink, K. König, K. Benndorf, C. Biskup, Fluorescence lifetime imaging by time-correlated single photon counting. Micr. Res. Techn. **63**, 58–66 (2004)
18. W. Becker, A. Bergmann, G. Biscotti, K. Koenig, I. Riemann, L. Kelbauskas, C. Biskup, High-speed FLIM data acquisition by time-correlated single photon counting. Proc. SPIE **5323**, 27–35 (2004)
19. W. Becker, *Advanced Time-Correlated Single-Photon Counting Techniques* (Springer, Berlin, 2005)
20. W. Becker, A. Bergmann, C. Biskup, Multi-spectral fluorescence lifetime imaging by TCSPC. Micr. Res. Tech. **70**, 403–409 (2007)

21. W. Becker, B. Su, A. Bergmann, Fast-acquisition multispectral FLIM by parallel TCSPC. Proc. SPIE **7183**, 718305 (2009)
22. W. Becker, The bh TCSPC handbook. 6th edition. Becker & Hickl GmbH (2015), www.becker-hickl.com, Printed copies available from Becker & Hickl GmbH
23. W. Becker, B. Su, A. Bergmann, Spatially resolved recording of transient fluorescence lifetime effects by line-scanning TCSPC. Proc. SPIE **8226**, 82260C-1–82260C-6 (2012)
24. W. Becker, Fluorescence lifetime imaging—techniques and applications. J. Microsc. **247**, 119–136 (2012)
25. W. Becker, V. Shcheslavkiy, S. Frere, I. Slutsky, Spatially resolved recording of transient fluorescence-lifetime effects by line-scanning TCSPC. Microsc. Res. Techn. **77**, 216–224 (2014)
26. M.Y. Berezin, S. Achilefu, Fluorescence lifetime measurement and biological imaging. Chem. Rev. **110**, 2641–2684 (2010)
27. D.J.S. Birch, A.S. Holmes, R.E. Imhof, B.Z. Nadolski, K. Suhling, Multiplexed array fluorometry. J. Phys. E. Sci Instrum. **21**, 415 (1988)
28. D.K. Bird, K.W. Eliceiri, C.-H. Fan, J.G. White, Simultaneous two-photon spectral and lifetime fluorescence microscopy. Appl. Opt. **43**, 5173–5182 (2004)
29. D.K. Bird, L. Yan, K.M. Vrotsos, K.E. Eliceiri, E.M. Vaughan, Metabolic mapping of MCF10A human breast cells via multiphoton fluorescence lifetime imaging of coenzyme NADH. Cancer Res. **65**, 8766–8773 (2005)
30. C. Biskup, T. Zimmer, L. Kelbauskas, B. Hoffmann, N. Klöcker, W. Becker, A. Bergmann, K. Benndorf, Multi-dimensional fluorescence lifetime and FRET measurements. Micr. Res. Tech. **70**, 403–409 (2007)
31. C. Biskup, B. Hoffmann, K. Benndorf, A. Rueck, Spectrally Resolved Lifetime Imaging Microscopy, in *FLIM Microscopy in Biology and Medicine*, ed. by A. Periasamy, R.M. Clegg (CRC Press, Boca Raton, 2009)
32. T.S. Blacker, Z.F. Mann, J.E. Gale, M. Ziegler, A.J. Bain, G. Szabadkai, M.R. Duchen, Separating NADH and NADPH fluorescence in live cells and tissues using FLIM. Nat. Commun. **5**, 3936-1–3936-6 (2014)
33. M. Böhmer, M. Wahl, H.-J. Rahn, R. Erdmann, J. Enderlein, Time-resolved fluorescence correlation spectroscopy. Chem. Phys. Lett. **353**, 439–445 (2002)
34. L.M. Bollinger, G.E. Thomas, Measurement of the time dependence of scintillation intensity by a delayed coincidence method. Rev. Sci. Instrum. **32**, 1044–1050 (1961)
35. J. Bordello, M. Novo, W. Al-Soufi, Exchange dynamics of a neutral hydrophobic dye in micellar solutions studied by fluorescence correlation spectroscopy. J. Colloid Interface Sci. **345**, 369–376 (2010)
36. J.W. Borst, S.P. Laptenok, A.H. Westphal, R. Kühnemuth, H. Hornen, N.V. Visser, S. Kalinin, J. Aker, A. van Hoek, C.A.M. Seidel, A.J.W.G. Visser, Structural changes of yellow cameleon domains observed by quantitative FRET analysis and polarized fluorescence correlation spectroscopy. Biophys. J. **95**, 5399–5411 (2008)
37. R. Brandenburg, H.-E. Wagner A. M. Morozov, K. V. Kozlov, Axial and radial development of microdischarges of barrier discharges in N_2/O_2 mixtures at atmospheric pressure. J. Phys. D: Appl. Phys. **38**, 1649–1657 (2005)
38. R. Brandenburg, H. Grosch, T. Hoder, K.-D. Weltmann, Phase resolved cross-correlation spectroscopy on surface barrier discharges in air at atmospheric pressure. Eur. Phys. J. Appl. Phys. **55**, 13813-p1–13813-p6 (2011)
39. C. Cheung, J.P. Culver, K. Takahashi, J.H. Greenberg, A.G. Yodh, In vivo cerebrovascular measurement combining diffuse near-infrared absorption and correlation spectroscopies. Phys. Med. Biol. **46**(8), 2053–2065 (2001)
40. D. Chorvat, A. Chorvatova, Spectrally resolved time-correlated single photon counting: a novel approach for characterization of endogenous fluorescence in isolated cardiac myocytes. Eur. Biophys. J. **36**, 73–83 (2006)

41. D. Chorvat, A. Mateasik, J. Kirchnerova, A. Chorvatova, Application of spectral unmixing in multi-wavelength time-resolved spectroscopy. Proc. SPIE **6771**, 677105-1–677105-12 (2007)
42. D. Chorvat, A. Chorvatova, Multi-wavelength fluorescence lifetime spectroscopy: a new approach to the study of endogenous fluorescence in living cells and tissues. Laser Phys. Lett. **6**, 175–193 (2009)
43. D. Chorvat Jr., A. Mateasik, Y.g Cheng, N.y Poirier, J. Miro, N.S. Dahdah, A. Chorvatova, Rejection of transplanted hearts in patients evaluated by the component analysis of multi-wavelength NAD(P)H fluorescence lifetime spectroscopy. J. Biophotonics **3**, 646–652 (2010)
44. A. Chorvatova, F. Elzwiei, A. Mateasik, D. Chorvat, Effect of ouabain on metabolic oxidative state in living cardiomyocytes evaluated by time-resolved spectroscopy of endogenous NAAD(P)H fluorescence. J. Biomed. Opt. **17**(10), 101505-1–101505-7 (2012)
45. A. Chorvatova, S. Aneba, A. Mateasik, D. Chorvat Jr., B. Comte, Time-resolved fluorescence spectroscopy investigation of the effect of 4-hydroxynonenal on endogenous NAD(P)H in living cardiac myocytes. J. Biomed. Opt. **18**(6), 067009-1–067009-11 (2013)
46. A. Chorvatova, A. Mateasik, D. Chorvat Jr, Spectral decomposition of NAD(P)H fluorescence components recorded by multi-wavelength fluorescence lifetime spectroscopy in living cardiac cells. Laser Phys. Lett. **10**, 125703-1–125703-10 (2013)
47. S. Coda, A.J. Thompson,1,5 G.T. Kennedy, K.L. Roche, L. Ayaru, D.S. Bansi, G.W. Stamp, A.V. Thillainayagam, P.M.W. French, C. Dunsby, Fluorescence lifetime spectroscopy of tissue autofluorescence in normal and diseased colon measured ex vivo using a fiber-optic probe. Biomed. Opt. Expr. **5**, 515–538 (2014)
48. D. Contini, A. Torricelli, A. Pifferi, L. Spinelli, F. Paglia, R. Cubeddu, Multi-channel time-resolved system for functional near infrared spectroscopy. Opt. Express **14**, 5418–5432 (2006)
49. R.J. Cooper, E. Magee, N. Everdell, S. Magazov, M. Varela, D. Airantzis, A.P. Gibson, J.C. Hebden, MONSTIR II: a 32-channel, multispectral, time-resolved optical tomography system for neonatal brain imaging. Rev. Sci. Instrum. **85**(5), 0531052014 (2014)
50. S. Cova, M. Bertolaccini, C. Bussolati, The measurement of luminescence waveforms by single-photon techniques. Phys. Stat. Sol. **18**, 11–61 (1973)
51. P.A.A. De Beule, C. Dunsby, N.P. Galletly, G.W. Stamp, A.C. Chu, U. Anand, P. Anand, C.D. Benham A. Naylor, P.M.W. French, A hyperspectral fluorescence lifetime probe for skin cancer diagnosis. Rev. Sci. Instrum. **78**, 123101 (2007)
52. M. Diez, B. Zimmermann, M. Börsch, M. König, E. Schweinberger, S. Steigmiller, R. Reuter, S. Fe-lekyan, V. Kudryavtchev, C.A.M. Seidel, P. Gräber, Proton-powered subunit rotation in single membrane-bound F0F1-ATP synthase. Nat. Struct. Mol. Biol. **11** (2), 135–141 (2004)
53. R.I. Dmitriev, A.V. Zhdanov, Y.M. Nolan, D.B. Papkovsky, Imaging of neurosphere oxygenation with phosphorescent probes. Biomaterials **34**, 9307–9317 (2013)
54. R.I. Dmitriev, A.V. Kondrashina, K. Koren, I. Klimant, A.V. Zhdanov, J.M.P. Pakan, K.W. McDermott, D.B. Papkovsky, Small molecule phosphorescent probes for O_2 imaging in 3D tissue models. Biomater. Sci. **2**, 853–866 (2014)
55. E. Dimitrow, I. Riemann, A. Ehlers, M.J. Koehler, J. Norgauer, P. Elsner, K. König, M. Kaatz, Spectral fluorescence lifetime detection and selective melanin imaging by multiphoton laser tomography for melanoma diagnosis. Exp. Dermatol. **18**, 509–515 (2009)
56. K. Drozdowicz-Tomsia, A.G. Anwer, M.A. Cahill, K.N. Madlum, A.M. Maki, M.S. Baker, E.M. Goldys, Multiphoton fluorescence lifetime imaging microscopy reveals free-to-bound NADH ratio changes associated with metabolic inhibition. J. Biomed. Opt. **19**, 08601 (2014)
57. M. Düser, Y. Bi, N. Zarrabi, S.D. Dunn, M. Börsch, The proton-translocating a subunit of F0F1-ATP synthase is allocated asymmetrically to the peripheral stalk. J. Biol. Chem. **48**, 33602–33610 (2008)
58. M. Düser, N.d Zarrabi, D.J. Cipriano, S. Ernst, G.D. Glick, S.D. Dunn, M. Börsch, 36° step size of proton-driven c-ring rotation in FoF1-ATP synthase. EMBO J. **28**, 2689–2696 (2009)

59. C. Dysli, G. Quellec, M Abegg, M.N. Menke, U. Wolf-Schnurrbusch, J. Kowal, J. Blatz, O. La Schiazza, A.B. Leichtle, S. Wolf, M.S. Zinkernagel, Quantitative analysis of fluorescence lifetime measurements of the macula using the fluorescence lifetime imaging ophthalmoscope in healthy subjects. IOVS **55**, 2107–2113 (2014)
60. S. Felekyan, R. Kühnemuth, V. Kudryavtsev, C. Sandhagen, W. Becker, C.A.M. Seidel, Full correlation from picoseconds to seconds by time-resolved and time-correlated single photon detection. Rev. Sci. Instrum. **76**, 083104 (2005)
61. S. Felekyan, Software package for multiparameter fluorescence spectroscopy, full correlation and multiparameter imaging. www.mpc.uni-duesseldorf.de/seidel/software.htm
62. S. Felekyan, S. Kalinin, A. Valeri, C.A.M. Seidel, Filtered FCS and species cross correlation function. Proc. SPIE **7183**, 71830D (2009)
63. Th. Förster, Zwischenmolekulare Energiewanderung und Fluoreszenz, Ann. Phys. (Serie 6) **2**, 55–75 (1948)
64. Th. Förster, Energy migration and fluorescence. Translated by Klaus Suhling. J. Biomed. Opt. **17**, 011002-1–011002-10
65. K. Funk, A. Woitecki, C. Franjic-Würtz, Th Gensch, F. Möhrlein, S. Frings, Modulation of chloride homeostasis by inflammatory mediators in dorsal ganglion neurons. Mol. Pain **4**, 32 (2008)
66. C.D. Geddes, H. Cao, I. Gryczynski, J. Fang, J.R. Lakowicz, Metal-enhanced fluorescence (MEF) due to silver colloids on a planar surface: Potential applications of indocyanine green to in vivo imaging. J. Phys. Chem. A **107**, 3443–3449 (2003)
67. V. Ghukassian, F.-J. Kao, Monitoring cellular metabolism with fluorescence lifetime of reduced nicotinamide adenine dinucleotide. J. Phys. Chem. C **113**, 11532–11540 (2009)
68. D. Gilbert, C. Franjic-Würtz, K. Funk, T. Gensch, S. Frings, F. Möhrlen, Differential maturation of chloride homeostasis in primary afferent neurons of the somatosensory system. Int. J. Devl. Neurosci. **25**, 479–489 (2007)
69. R. Govindjee, Sixty-three years since Kautsky: chlorophyll α fluorescence, Aust. J. Plant Physiol. **22**, 131–160 (1995)
70. D. Granadero, J. Bordello, M.J. Perez-Alvite, M. Novo, W. Al-Soufi, Host-guest complexation studied by fluorescence correlation spectroscopy: adamantane-cyclodextrin inclusion. Int. J. Mol. Sci. **11**, 173–188 (2010)
71. H. Grosch, T. Hoder, K.-D. Weltmann, R. Brandenburg, Spatio-temporal development of microdischarges in a surface barrier discharge arrangement in air at atmospheric pressure. Eur. Phys. J. D **60**, 547–553 (2010)
72. R. Hanbury-Brown, R.Q. Twiss, Nature **177**, 27–29 (1956)
73. K.M. Hanson, M.J. Behne, N.P. Barry, T.M. Mauro, E. Gratton, Two-photon fluorescence imaging of the skin stratum corneum pH gradient. Biophys. J. **83**, 1682–1690 (2002)
74. T. Hoder, R. Brandenburg, R. Basner1, K.-D. Weltmann, K.V. Kozlov, H.-E. Wagner, A comparative study of three different types of barrier discharges in air at atmospheric pressure by cross-correlation spectroscopy. J. Phys. D: Appl. Phys. **43**, 124009-1–124009-8 (2010)
75. T. Hoder, M. Cernak, J. Paillol, D. Loffhagen, R. Brandenburg, High-resolution measurements of the electric field at the streamer arrival to the cathode: A unification of the streamer-initiated gas-breakdown mechanism. Phys. Rev. E **86**, 055401-1–055401-5 (2012)
76. M. Kacprzak, A. Liebert, P. Sawosz, N. Zolek, R. Maniewski, Time-resolved optical imager for assessment of cerebral oxygenation. J. Biomed. Opt. **12**, 034019-1–034019-14 (2007)
77. H. Kaneko, I. Putzier, S. Frings, U.B. Kaupp, Th Gensch, Chloride accumulation in mammalian olfactory sensory neurons. J. Neurosci. **24**(36), 7931–7938 (2004)
78. S.R. Kantelhardt, J. Leppert, J. Krajewski, N. Petkus, E. Reusche, V. M. Tronnier, G. Hüttmann, A. Giese, Imaging of brain and brain tumor specimens by time-resolved multiphoton excitation microscopy ex vivo. Neuro-Onkology **9**, 103–112 (2007)
79. V. Katsoulidou, A. Bergmann, W. Becker, How fast can TCSPC FLIM be made? Proc. SPIE **6771**, 67710B-1–67710B-7 (2007)

80. L. Kelbauskas, W. Dietel, Internalization of aggregated photosensitizers by tumor cells: Subcellular time-resolved fluorescence spectroscopy on derivatives of pyropheophorbide-a ethers and chlorin e6 under femtosecond one- and two-photon excitation. Photochem. Photobiol. **76**, 686–694 (2002)
81. S. Khoon Teh, W. Zheng, S. Li, D. Li, Y. Zeng, Y. Yang, J. Y. Qu, Multimodal nonlinear optical microscopy improves the accuracy of early diagnosis of squamous intraepithelial neoplasia. J. Biomed. Opt. **18**(3), 036001-1–036001-11 (2013)
82. P. Kloc, H.-E. Wagner, D. Trunec, Z. Navratil, G. Fedosev, An investigation of dieclectric barrier dis-charge in Ar and Ar/NH_3 mixture using cross-correlation spectroscopy. J. Phys. D Appl. Phys. **43**, 34514–345205 (2010)
83. M. Köllner, J. Wolfrum, How many photons are necessary for fluorescence-lifetime measurements? Phys. Chem. Lett. **200**, 199–204 (1992)
84. K. König, Clinical multiphoton tomography. J. Biophoton. **1**, 13–23 (2008)
85. K. Koenig, A. Uchugonova, in *Multiphoton Fluorescence Lifetime Imaging at the Dawn of Clinical Application*, ed by A. Periasamy, R.M. Clegg, FLIM Microscopy in Biology and Medicine (CRC Press, Boca Raton, 2009)
86. K. König, A. Uchugonova, E. Gorjup, Multiphoton fluorescence lifetime imaging of 3D-stem cell spheroids during differentiation. Microsc. Res. Techn. **74**, 9–17 (2011)
87. K.V. Kozlov, R. Brandenburg, H.-E. Wagner, A.M. Morozov, P. Michel, Investigation of the filamentary and diffuse mode of barrier discharges in N2/O2 mixtures at atmospheric pressure by cross-correlation spectroscopy. J. Phys. D Appl. Phys. **38**, 518–529 (2005)
88. K.V. Kuchibhotla, C.R. Lattarulo, B. Hyman, B. J. Bacskai, Synchronous hyperactivity and intercellular calcium waves in astrocytes in Alzheimer mice. Science **323**, 1211–1215 (2009)
89. M.K. Kuimova, G. Yahioglu, J.A. Levitt, K. Suhling, Molecular rotor measures viscosity of live cells via fluorescence lifetime imaging. J. Am. Chem. Soc. **130**, 6672–6673 (2008)
90. J.R. Lakowicz, H. Szmacinski, M.L. Johnson, Calcium imaging using fluorescence lifetimes an long-wavelength probes. J. Fluoresc. **2**, 47–62 (1992)
91. J.R. Lakowicz, H. Szmacinski, K. Nowaczyk, M.L. Johnson, Fluorescence lifetime imaging of free and protein-bound NADH. PNAS **89**, 1271–1275 (1992)
92. J.R. Lakowicz, *Principles of Fluorescence Spectroscopy*, 3rd edn. (Springer, Berlin, 2006)
93. G.S. Lakshmikanth, G. Krishnamoorthy, Solvent-exposed tryptophans probe the dynamics at protein surfaces. Biophys. J. **77**, 1100–1106 (1999)
94. G.S. Lakshmikanth, K. Sridevi, G. Krishnamoorthy, J.B. Udgaonkar, Structure is lost incrementally during the unfolding of barstar. Nat. Struct. Biol. **8**, 799–804 (2001)
95. J. Leppert, J. Krajewski, S.R. Kantelhardt, S. Schlaffer, N. Petkus, E. Reusche, G. Hüttmann, A. Giese, Multiphoton excitation of autofluorescence for microscopy of glioma tissue. Neurosurgery **58**, 759–767 (2006)
96. B. Leskovar, C.C. Lo, Photon counting system for subnanosecond fluorescence lifetime measurements. Rev. Sci. Instrum. **47**, 1113–1121 (1976)
97. C. Lewis, W.R. Ware, The measurement of short-lived fluorescence decay using the single photon counting method. Rev. Sci. Instrum. **44**, 107–114 (1973)
98. D. Li, W. Zheng, J.Y. Qu, Time-resolved spectroscopic imaging reveals the fundamentals of cellular NADH fluorescence. Opt. Lett. **33**, 2365–2367 (2008)
99. D. Li, M.S. Yang, W. Zheng, J.Y. Qu, Study of cadmium-induced cytotoxicity using two-photon excitation endogenous fluorescence microscopy. J. Biomed. Opt. **14**(5), 054028-1–054028-8 (2009)
100. D. Li, W. Zheng, .J.Y. Qu, Two-photon autofluorescence microscopy of multicolor excitation. Opt. Lett. **34**, 202–204 (2009)
101. D. Li, W. Zheng, .J.Y. Qu, Imaging of epithelial tissue in vivo based on excitation of multiple endogenous nonlinear optical signals. Letter **34**, 2853–2855 (2009)
102. D. Li, W. Zheng, Y. Zeng, and J. Y. Qu, In vivo and simultaneous multimodal imaging: Integrated multiplex coherent anti-Stokes Raman scattering and two-photon microscopy. Appl. Phys. Lett **97**, 223702-1–223702-3 (2010)

103. D. Li, W. Zheng, Y. Zeng, Y. Luo, J.Y. Qu, Two-photon excited hemoglobin fluorescence provides contrast mechanism for label-free imaging of microvasculature in vivo. Opt. Lett. **36**, 834–836 (2011)
104. D. Li, W. Zheng, W. Zhang, S. Khoon Teh, Y. Zeng, Y. Luo, J.Y. Qu, Time-resolved detection enables standard two-photon fluorescence microscopy for in vivo label-free imaging of microvasculature in tissue. Opt. Lett. **36**, 2638–2640 (2011)
105. A. Liebert, H. Wabnitz, M. Möller, A. Walter, R. Macdonald, H. Rinneberg, H. Obrig, I. Steinbrink, Time-Resolved Diffuse NIR-Reflectance Topography of the Adult Head During Motor Stimulation, in *OSA Biomedical Optics Topical Meetings on CD ROM* (The Optical Society of America, Washington, DC, WF34 2004)
106. A. Liebert, H. Wabnitz, J. Steinbrink, H. Obrig, M. Möller, R. Macdonald, A. Villringer, H. Rinneberg, Time-resolved multidistance near-infrared spectroscopy at the human head: Intra- and extracerebral absorption changes from moments of distribution of times of flight of photons. Appl. Opt. **43**, 3037–3047 (2004)
107. A. Liebert, H. Wabnitz, J. Steinbrink, M. Möller, R. Macdonald, H. Rinneberg, A. Villringer, H. Obrig, Bed-side assessment of cerebral perfusion in stroke patients based on optical monitoring of a dye bolus by time-resolved diffuse reflectance. NeuroImage **24**, 426–435 (2005)
108. A. Liebert, P. Sawosz, D. Milej, M. Kacprzak, W. Weigl, M. Botwicz, J. Maczewska, K. Fronczewska, E. Mayzner-Zawadzka, L. Krolicki, R. Maniewski, Assessment of inflow and washout of indocyanine green in the adult human brain by monitoring of diffuse reflectance at large source-detector separation. J. Biomed. Opt. **16**(4), 046011-1–046011-7 (2011)
109. J. Malicka, I. Gryczynski, C.D. Geddes, J.R. Lakowicz, Metal-enhanced emission from indocyanine green: a new approach to in vivo imaging. J. Biomed. Opt. **8**, 472–478 (2003)
110. W. Meiling, F. Stary, *Nanosecond Pulse Techniques* (Akademie-Verlag, Berlin, 1963)
111. D. Milej, A. Gerega, N. Zolek, W. Weigl, M. Kacprzak, P. Sawosz, J. Maczewska, K. Fronczewska, E. Mayzner-Zawadzka, L. Krolicki, R. Maniewski, A. Liebert, Time-resolved detection of fluorescent light during inflow of ICG to the brain—a methodological study. Phys. Med. Biol. **57**, 6725–6742 (2012)
112. A. Minta, J.P.Y. Kao, R.Y. Tsien, Fluorescent indicators for cytosolic calcium based on rhodamine and fluorescein chromophores. J. Biol. Chem. **264**, 8171–8178 (1989)
113. H.S. Muddana, T.T. Morgan, J.H. Adair, P.J. Butler, Photophysics of Cy3-encapsulated calcium phosphate nanoparticles. Nano Lett. **9**(4), 1556–1559 (2009)
114. S. Mukhopadhyay, P.K. Nayak, J.B. Udgaonkar, G. Krishnamoorthy, Characterization of the formation of amyloid Protofibrils from Barstar by mapping residue-specific fluorescence dynamics. J. Mol. Biol. **358**, 935–942 (2006)
115. T.A. Nguyen, P. Sarkar, J.V. Veetil, S.V. Koushik, S.S. Vogel, Fluorescence polarization and fluctuation analysis monitors subunit proximity, stoichiometry, and protein complex hydrodynamics. PLoS ONE **7**, e38209-1–e38209-13 (2012)
116. M. Novo, S. Felekyan, C.A.M. Seidel, W. Al-Soufi, Dye-exchange dynamics in micellar solutions studied by fluorescence correlation spectroscopy. J. Phys. Chem. B **111**, 3614–3624 (2007)
117. D.V. O'Connor, D. Phillips, *Time-Correlated Single Photon Counting* (Academic Press, London, 1984)
118. S. Pallikkuth, D.J. Blackwell, Z. Hu, Z. Hou, D.T. Zieman, B. Svensson, D.D. Thomas, S.L. Robia, Phosphorylated phospholamban stabilizes a compact conformation of the cardiac calcium-ATPase. Biophys. J. **105**, 1812–1821 (2013)
119. R.J. Paul, H. Schneckenburger, Oxygen concentration and the oxidation-reduction state of yeast: determination of free/bound NADH and flavins by time-resolved spectroscopy. Naturwissenschaften **83**, 32–35 (1996)
120. J.P. Philip, K. Carlsson, Theoretical investigation of the signal-to-noise ratio in fluorescence lifetime imaging. J. Opt. Soc. Am. **A20**, 368–379 (2003)

121. M. Prummer, C. Hübner, B. Sick, B. Hecht, A. Renn, U.P. Wild, Single-molecule identification by spectrally and time-resolved fluorescence detection. Anal. Chem. **72**, 433–447 (2000)
122. R. Re, D. Contini, M. Caffini, R. Cubeddu, L. Spinelli, A. Torricelli, A compact time-resolved system for near infrared spectroscopy based on wavelength space multiplexing. Rev. Sci. Instrum. **81**, 113101 (2010)
123. R. Rigler, E.S. Elson (eds.), *Fluorescence Correlation Spectroscopy* (Springer, Berlin, 2001)
124. T. Ritman-Meer, N.I. Cade, D. Richards, Spatial imaging of modifications to fluorescence lifetime and intensity by individual Ag nanoparticles. Appl. Phys. Lett. **91**, 123122 (2007)
125. M.S. Roberts, Y. Dancik, T.W. Prow, C.A. Thorling, L. Li, J.E. Grice, T.A. Robertson, K. König, W. Becker, Non-invasive imaging of skin physiology and percutaneous penetration using fluorescence spectral and lifetime imaging with multiphoton and confocal microscopy. Eur. J. Pharm. Biopharm. **77**, 469–488 (2011)
126. A. Rück, F. Dolp, C. Hülshoff, C. Hauser, C. Scalfi-Happ, Fluorescence lifetime imaging in PDT. An overview. Med. Laser Appl. **20**, 125–129 (2005)
127. A. Rück, Ch. Hülshoff, I. Kinzler, W. Becker, R. Steiner, SLIM: a new method for molecular imaging. Micr. Res. Tech. **70**, 403–409 (2007)
128. A. Rück, C. Hauser, S. Mosch, S. Kalinina, Spectrally resolved fluorescence lifetime imaging to investigate cell metabolism in malignant and nonmalignant oral mucosa cells. J. Biomed. Opt. **19**(9), 096005-1–096005-9 (2014)
129. S. Sakadžic, E. Roussakis, M.A. Yaseen, E.T. Mandeville, V.J. Srinivasan1, K. Arai, S. Ruvinskaya, A. Devor, E.H. Lo, S.A. Vinogradov, D.A. Boas, Two-photon high-resolution measurement of partial pressure of oxygen in cerebral vasculature and tissue. Nat. Methods **7**(9), 755–759 (2010)
130. R. Sanders, A. Draaijer, H.C. Gerritsen, P.M. Houpt, Y.K. Levine, Quantitative pH Imaging in cells using confocal fluorescence lifetime imaging microscopy. Anal. Biochem. **227**, 302–308 (1995)
131. W.Y. Sanchez, T.W. Prow, W.H. Sanchez, J.E. Grice, M.S. Roberts, Analysis of the metaboloic deterioration of ex-vivo skin, from ischemic necrosis, through the imaging of intracellular NAD(P)H by multiphoton tomography and fluorescence lifetime imaging microscopy (MPT-FLIM). J. Biomed. Opt. 09567RR in press (2010)
132. A.M. Saxena, J.B. Udgaonkar, G. Krishnamoorthy, Characterization of intra-molecule distances ans site-specific dynamics in chemically unfolded barstar: Evidence for denaturant-dependent non-random structure. J. Mol. Biol. **359**, 174–189 (2006)
133. R. Schuyler, I. Isenberg, A monophoton fluorometer with energy discrimination. Rev. Sci. Instrum. **42**, 813–817 (1971)
134. D. Schweitzer, A. Kolb, M. Hammer, E. Thamm, Basic investigations for 2-dimensional time-resolved fluorescence measurements at the fundus. Int. Ophthalmol. **23**, 399–404 (2001)
135. D. Schweitzer, S. Schenke, M. Hammer, F. Schweitzer, S. Jentsch, E. Birckner, W. Becker, Towards metabolic mapping of the human retina. Micr. Res. Tech. **70**, 403–409 (2007)
136. D. Schweitzer, Metabolic Mapping, in *Medical Retina, Essential in Opthalmology*, ed. by F. G. Holz, R.F. Spaide (Springer, New York, 2010)
137. M.C. Skala, K.M. Riching, D.K. Bird, A. Dendron-Fitzpatrick, J. Eickhoff, K.W. Eliceiri, P J. Keely, N. Ramanujam, In vivo multiphoton fluorescence lifetime imaging of protein-bound and free nicotinamide adenine dinucleotide in normal and precancerous epithelia. J. Biomed. Opt. **12**, 02401-1–02401-10 (2007)
138. M.C. Skala, K.M. Riching, A. Gendron-Fitzpatrick, J. Eickhoff, K.W. Eliceiri, J.G. White, N. Ramanujam, In vivo multiphoton microscopy of NADH and FAD redox states, fluorescence lifetimes, and cellular morphology in precancerous epithelia. PNAS **104**, 19494–19499 (2007)
139. H. Studier, W. Becker, Megapixel FLIM. Proc. SPIE **8948**, 89481K (2014)
140. K. Suhling, D. McLoskey, D.J.S. Birch, Multiplexed single-photon counting. II. The statistical theory of time-correlated measurements. Rev. Sci. Instrum. **67**, 2230–2246 (1996)

141. Q. Sun, Y. Li, S. He, C. Situ, Z. Wu, J.Y. Qu, Label-free multimodal nonlinear optical microscopy reveals fundamental insights of skeletal muscle development. Biomed. Opt. Expr. **5**, 158–166 (2013)
142. C. Thaler, S.V. Koushik, H.L. Puhl, P.S. Blank, S.S. Vogel, Structural rearrangement of CaMKIIα catalytic domains encodes activation. PNAS **106**, 6369–6374 (2009) doi:10.1073/pnas.0901913106
143. Tregido, J.A. Levitt, K. Suhling, Effect of refractive index on the fluorescence lifetime of green fluorescent protein. J. Biomed. Opt. **13**(3), 031218-1–031218-8 (2008)
144. S.S. Vogel, C. Thaler, P.S. Blank, S.V. Koushik, Time-Resolved Fluorescence Anisotropy, ed by A. Periasamy, R.M. Clegg, FLIM Microscopy in Biology and Medicine (CRC Press, Taylor & Francis, Boca Raton, 2010)
145. H.E. Wagner, R. Brandenburg, K.V. Kozlov, Progress in the visualisation of filamentary gas discharges, part1: milestones and diagnostics of dielectric-barrier discharges by cross-correlation. J. Adv. Oxid. Technol. **7**, 11–19 (2004)
146. A.J. Walsh, R.S. Cook, H.C. Manning, D.J. Hicks, A. Lafontant, C.L. Arteaga, M.C. Skala, Optical metabolic imaging identifies glycolytic levels, subtypes, and early-treatment response in breast cancer. Cancer Res. **73**, 6164–6174 (2013)
147. A.J. Walsh, R.S. Cook, M.E. Sanders, L. Aurisicchio, G. Ciliberto, C.L. Arteaga, M.C. Skala, Quantitative optical imaging of primary tumor organoid metabolism predicts drug response in breast cancer. Cancer Res. **74**, OF1-OF11 (2014)
148. H-W. Wang, V. Ghukassyan, C.T. Chen, Y.H. Wei, H.W. Guo, J.S. Yu, F.J. Kao, Differentiation of apoptosis from necrosis by dynamic changes of reduced nicotinamide adenine dinucleotide fluorescence lifetime in live cells. J. Biomed. Opt. **13**(5), 054011-1–054011-9 (2008)
149. J. Widengren, V. Kudryavtsev, M. Antonik, S. Berger. M. Gerken, C.A.M. Seidel, Single-molecule detection and identification of multiple species by multiparameter fluorescence detection. Anal. Chem. **78**, 2039–2050 (2006)
150. M.S. Yang, D. Li, T, Lin, J.J. Zheng, W. Zheng, J.Y. Qu, Increase in intracellular free/bound NAD[P]H as a cause of Cd-induced oxidative stress in the $HepG_2$ cells. Toxicology **247**, 6–10 (2008)
151. J. Yguerabide, Nanosecond fluorescence spectroscopy of macromolecules. Meth. Enzymol. **26**, 498–578 (1972)
152. Y. Zeng, B. Yan, Q. Sun, S. Khoon Teh, W. Zhang, Z. Wen, Jianan Y. Qu, Label-free in vivo imaging of human leukocytes using two-photon excited endogenous fluorescence. J. Biomed. Opt. **18**(4), 040103-1–040103-3 (2013)
153. W. Zheng, D. Li, J.Y. Qu, Monitoring changes of cellular metabolism and microviscosity in vitro based on time-resolved endogenous fluorescence and its anisotropy decay dynamics. J. Biomed. Opt. **15**(3), 037013-1–037013-11 (2010)
154. W. Zheng, D. Li, Y. Zeng, Y. Luo, J.Y. Qu, Two-photon excited hemoglobin fluorescence. Biomed. Opt. Expr. **2**, 71–79 (2011)

http://www.springer.com/978-3-319-14928-8

Advanced Time-Correlated Single Photon Counting Applications

Becker, W. (Ed.)

2015, XXIII, 624 p. 321 illus., 214 illus. in color.,
Hardcover
ISBN: 978-3-319-14928-8